electronics

MDPI

Article

Intelligent Charging Reservation and Trip Planning of CAEVs and UAVs

Palwasha W. Shaikh, Hussein T. Mouftah and Burak Kantarci *

School of Electrical Engineering and Computer Science, University of Ottawa, Ottawa, ON K1N 6N5, Canada; pshai065@uottawa.ca (P.W.S.)
* Correspondence: burak.kantarci@uottawa.ca

Abstract

Connected and Autonomous Electric Vehicles (CAEVs) and Uncrewed Aerial Vehicles (UAVs) are critical components of future Intelligent Transportation Systems (ITS), yet their deployment remains constrained by fragmented charging infrastructures and the lack of coordinated reservation and trip planning across static, dynamic wireless, and vehicle-to-vehicle (V2V) charging networks using magnetic resonance and laser-based power transfer. Existing solutions often struggle with misalignment sensitivity, unpredictable arrivals, and disconnected ground–aerial scheduling. This work introduces a three-layer architecture that integrates a handshake protocol for coordinated charging and billing, a misalignment correction algorithm for magnetic resonance and laser-based systems, and three scheduling strategies: Static Heuristic Charging Scheduling and Planning (SH-CSP), Dynamic Heuristic Charging Scheduling and Planning (DH-CSP), and the Safety, Scheduling, and Sustainability-Aware Feasibility-Enhanced Deep Deterministic Policy Gradient (SAFE-DDPG). SAFE-DDPG extends vanilla DDPG with feasibility-aware action filtering, prioritized replay, and adaptive exploration to enable real-time scheduling in heterogeneous and congested charging networks. Results show that SAFE-DDPG significantly improves scheduling efficiency, reducing average wait times by over 70% compared to DH-CSP and over 85% compared to SH-CSP, demonstrating its potential to support scalable and coordinated ground–aerial charging ecosystems.

Keywords: connected autonomous electric vehicles; unmanned aerial vehicles; dynamic wireless charging; charging reservation; trip planning; deep reinforcement learning; intelligent transportation systems

Check for updates

Academic Editors: Jonas Matijosius, Kristina Čižiūnienė and Metin Mutlu Aydın

Received: 4 December 2025
Revised: 9 January 2026
Accepted: 9 January 2026
Published: 19 January 2026

Copyright: © 2026 by the authors. Licensee MDPI, Basel, Switzerland. This article is an open access article distributed under the terms and conditions of the Creative Commons Attribution (CC BY) license.

1. Introduction

Connected and Autonomous Electric Vehicles (CAEVs) [1–4] are poised to play a central role in future Intelligent Transportation System (ITS) by enabling autonomous and electrified ground mobility. In parallel, Uncrewed Aerial Vehicles (UAVs) [5–8] provide flexible aerial transportation capabilities for a wide range of smart-city applications. Together, CAEVs and UAVs are expected to underpin next-generation transportation ecosystems through enhanced connectivity, automation, and service flexibility [5,9–11]. Their integration into shared mobility systems can improve efficiency, reduce emissions, and enhance service reliability. However, realizing these benefits in practice requires effective coordination across heterogeneous charging infrastructures and ground–aerial platforms, a challenge that remains insufficiently addressed in existing studies [1–3,5,12,13]. Despite these advances, existing studies predominantly address CAEVs and UAVs as separate

systems, overlooking the coupling between ground and aerial vehicles when they share charging infrastructure, scheduling resources, and access control mechanisms. This work addresses this gap by proposing a unified CAEV–UAV charging and trip-planning framework that explicitly accounts for heterogeneous charging technologies, dynamic arrivals, and adaptive coordination requirements, with an emphasis on system-level coordination across shared charging, scheduling, and access-control resources.

The complexity is further heightened in heterogeneous vehicular networks, which encompass not only diverse vehicle types but also variations in communication standards, power transfer methods, hardware capabilities, and battery characteristics. Differences in how vehicles deplete energy, communicate with infrastructure, or receive power through static plug-in systems, wireless transfer, or optical beams create highly irregular and dynamic operating conditions. Coordinated scheduling and resource allocation under such conditions require adaptive strategies that conventional approaches cannot adequately address [3,4,9]. Recent work on UAV-enabled wireless powered communication networks and UAV trip planning has examined trajectory optimization, Age-of-Information (AoI) minimization, and joint transmission–trajectory co-design. While these studies focus on communication and flight-path optimization for aerial systems, they do not address coordinated charging scheduling or shared infrastructure management across ground and aerial vehicles.

Figure 1 illustrates the open challenges in charging and scheduling for CAEVs and UAVs. It highlights the lack of integrated ground–aerial coordination, insufficient support for diverse charging technologies and systems, sensitivity to misalignment during wireless power transfer, complications from early or late vehicle arrivals, limited real-time responsiveness, and the absence of integrated billing and access control. Addressing these gaps requires a unified framework capable of dynamically coordinating heterogeneous charging resources while adapting to uncertain network conditions, particularly when ground and aerial vehicles compete for shared energy, reservation, and scheduling resources. Specifically, the proposed framework addresses these challenges through joint ground–aerial coordination via a shared reservation and billing handshake, misalignment-aware wireless charging correction, and progressively adaptive scheduling strategies. These components collectively mitigate uncertainty arising from heterogeneous charging technologies, mobility-induced misalignment, and stochastic vehicle arrivals.

To tackle these challenges and explicitly coordinate shared energy, scheduling, and reservation resources across ground and aerial domains, we propose a three-layer scheduling framework that unifies CAEV and UAV charging coordination. Specifically, Static Heuristic Charging Scheduling and Planning (SH-CSP) provides a static heuristic baseline, Dynamic Heuristic Charging Scheduling and Planning (DH-CSP) extends this model to handle dynamic arrivals through rolling re-optimization, and Safety, Scheduling, and Sustainability-Aware Feasibility-Enhanced Deep Deterministic Policy Gradient (SAFE-DDPG) further generalizes coordination by learning adaptive policies under uncertainty while enforcing feasibility constraints. Together, these strategies form a progressive hierarchy spanning static, dynamic, and learning-based scheduling within a unified framework. The framework incorporates a handshake protocol for billing and reservation and a misalignment-aware correction mechanism for magnetic resonance and laser-based charging. Central to this framework is the SAFE-DDPG algorithm, an enhanced Deep Reinforcement Learning (DRL)-based scheduler designed to enable adaptive decision-making in heterogeneous and congested charging networks.

Motivated by the tight coupling of ground and aerial vehicles through shared charging and scheduling resources, which remains unaddressed by existing isolated approaches, this work makes the following key contributions:

- Unified Ground-Aerial Scheduling Framework: Development of an integrated architecture that jointly manages charging and reservations for CAEVs and UAVs across heterogeneous infrastructures, addressing the lack of ground–aerial coordination highlighted in Figure 1.
- Misalignment-Aware Energy Management: Design of a correction mechanism that reduces energy transfer losses and improves reliability of magnetic resonance and laser-based wireless charging.
- Feasibility-Aware Deep Reinforcement Learning: Introduction of SAFE-DDPG, an enhanced DRL-based scheduler that extends Deep Deterministic Policy Gradient (DDPG) with feasibility-aware action filtering, prioritized replay, and adaptive exploration, enabling superior performance under uncertain arrivals, infrastructure constraints, and dynamic network conditions.
- Quantitative Outcomes: Results demonstrate substantial reductions in vehicle wait times, travel times, and battery consumption while maintaining high charging efficiency under diverse network scenarios.

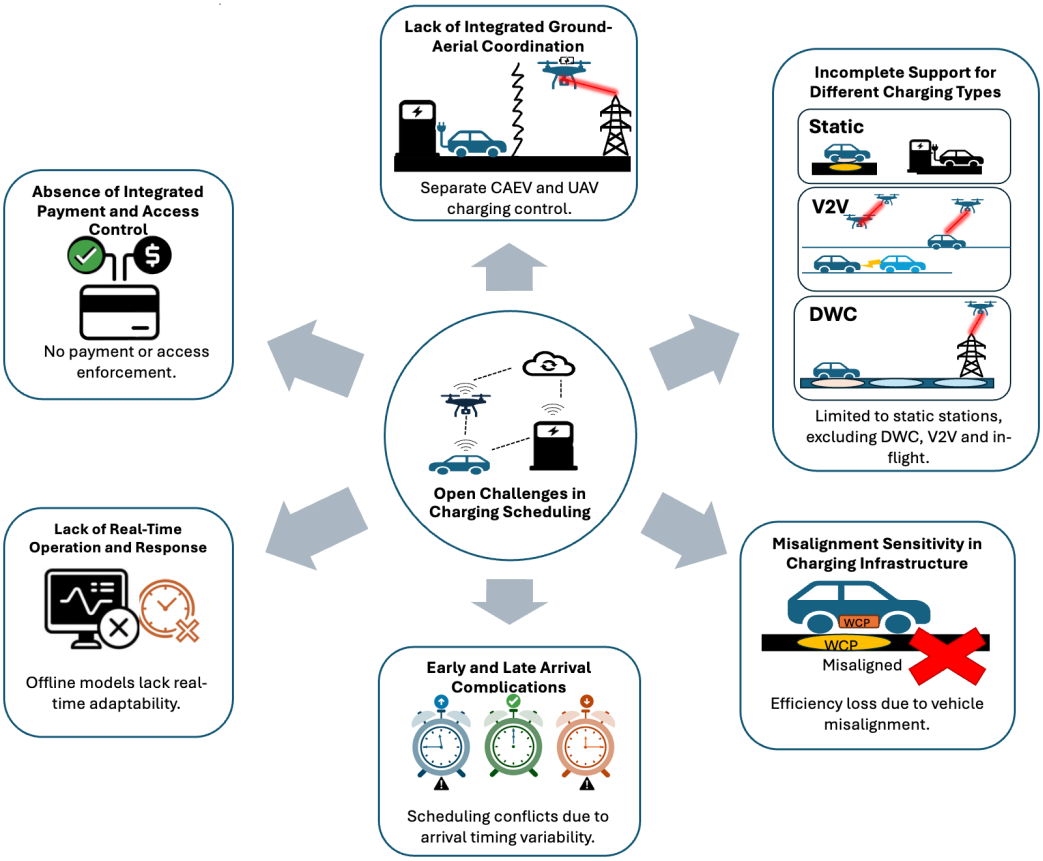


Figure 1. Open challenges in charging scheduling for CAEVs and UAVs.

The remainder of this paper is organized as follows. Section 2 reviews charging technologies for CAEVs and UAVs and surveys state-of-the-art DRL-based approaches for scheduling, routing, and energy management. Section 3 presents the proposed three-layer scheduling framework, including the secure handshake protocol, power and communication models, battery management, charging reservation and trip planning, misalignment correction algorithm, and dynamic arrival handling. This section also details two heuristic scheduling algorithms and the modified DDPG approach with feasibility-aware filtering, fallback mechanisms, prioritized replay, and an adaptive exploration strategy. Section 4 describes the simulation setup and evaluates the proposed heuristic and learning-based

algorithms, including scalability of the modified DDPG, comparison with vanilla DDPG, and a mechanism-level ablation analysis.

2. Background and Related Work

2.1. Background and Charging Technologies

The global transition to sustainable transportation is accelerating due to mounting concerns over greenhouse gas emissions and climate change. In Canada, the transportation sector alone produced approximately 156 megatons of CO_2 emissions in 2024 [14], underscoring the need for innovative mobility solutions [15]. CAEVs [1–3] and UAVs [5,13] are two critical technologies driving this transition, which is essential to achieving net-zero carbon emissions by 2050 [15,16]. CAEVs combine electric propulsion with advanced sensing, communication, and decision-making capabilities, enabling autonomous operation and optimized energy use [3,4]. Meanwhile, UAVs are increasingly deployed for applications such as last-mile logistics, environmental monitoring, and emergency response, provide operational flexibility and reach in scenarios where ground transportation is less effective [6–8,12,17–20].

Both technologies are central to the evolution of future ITS [9–11,20], which integrate communication, automation, and real-time decision-making to improve transportation efficiency and sustainability. However, their large-scale adoption faces persistent challenges. CAEVs often encounter range limitations, long charging times, and station congestion, while UAVs are restricted by limited onboard energy storage and the lack of continuous charging infrastructure. Furthermore, existing energy ecosystems remain fragmented, relying on vehicle-specific charging systems that operate independently. The absence of a unified energy management framework that integrates both ground and aerial platforms limits scalability and hinders efficient energy distribution.

Efficient energy replenishment is therefore a critical enabler for future mobility. CAEVs and UAVs rely on several charging technologies, each offering unique advantages and trade-offs in terms of efficiency, infrastructure complexity, flexibility, and operational continuity. Traditional wired charging remains the most widely used approach, providing high efficiency through direct physical connectors. However, it requires vehicles to stop and manually connect, thus reducing operational flexibility. Static Wireless Charging (SWC), based on Inductive Power Transfer (IPT) or Capacitive Power Transfer (CPT) power transfer, eliminates the need for physical contact and enhances user convenience. IPT systems, commonly installed in parking areas and dedicated charging hubs, require precise alignment, and efficiency drops significantly with increased air gaps or high-frequency operation [21]. CPT offers lower efficiency and is typically suitable for low-power applications [21]. For UAVs, SWC implementations typically require landing or hovering near charging pads, which reduces flight duration and introduces safety challenges associated with high-voltage systems [5,9].

Dynamic Wireless Charging (DWC) extends operational flexibility by enabling vehicles to receive energy while in motion. For CAEVs, this involves embedding transmitter coils beneath road surfaces, reducing dependency on fixed charging stops and supporting long-distance travel. UAVs can employ Optical Wireless Power Transfer (OWPT) using laser beams to recharge in flight, eliminating many alignment constraints and achieving energy transfer over longer distances. Experiments show that OWPT can deliver up to 16.29 kWh over several kilometers [22], although environmental factors such as fog or rain can reduce performance, and safety constraints must be carefully managed. Emerging solutions such as Vehicle-to-Vehicle (V2V) charging allow direct energy transfer between CAEVs or between ground and aerial vehicles, reducing reliance on fixed infrastructure and supporting cooperative energy use in distributed networks. However, these approaches introduce new

challenges related to coordination, safety, and scheduling. Comparable scheduling and charging optimization problems have been addressed in wireless sensor networks, where mobile chargers plan dynamic paths to service distributed nodes efficiently [23].

Despite these advances, integrating diverse charging technologies into a unified infrastructure remains an open challenge. Realizing such an integrated system requires intelligent scheduling, real-time decision-making, and efficient resource allocation to manage spatial, temporal, and energy constraints across heterogeneous platforms. Addressing these challenges is essential for enabling scalable, coordinated, and efficient electric mobility ecosystems.

Emerging communication and computing technologies, including sixth-generation (6G) wireless networks [10,11,24,25], the Internet of Things (IoT), and Intelligent Edge Computing (IEC) [26–31], form the digital backbone of future ITS. They provide ultra-reliable low-latency communication, massive device interconnection, and localized intelligence. These advances enable coordination across heterogeneous platforms such as CAEVs and UAVs, yet their potential remains underutilized because of fragmented infrastructure, fluctuating energy demands, and stringent real-time scheduling requirements. Despite progress in individual charging technologies, existing solutions remain fragmented, typically addressing ground or aerial platforms in isolation. As a result, coordination challenges related to shared infrastructure, heterogeneous charging modalities, and coupled scheduling decisions across CAEVs and UAVs systems remain remain open. This motivates an integrated charging and scheduling framework for joint ground–aerial energy management. The proposed three-layer architecture enables modular coordination across heterogeneous charging technologies and vehicle types while maintaining scalability and real-time operability.

Table 1 summarizes the characteristics of key charging technologies for CAEVs and UAVs. Figure 2 illustrates their deployment across a unified charging ecosystem.

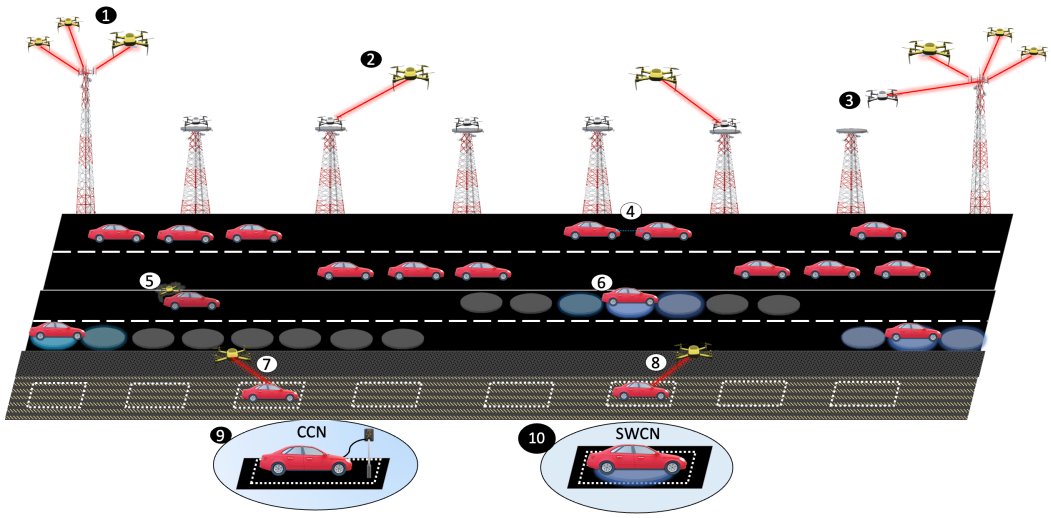


Figure 2. System overview of CAEV and UAV charging methods: (1) laser beaming UAV charged from tower, (2) laser beaming UAV-to-UAV transfer, (3) edge intelligent UAV receiving tower charging, (4) CAEV-to-CAEV charging, (5) magnetic resonance charging UAV-to-CAEV, (6) dynamic wireless charging for CAEV, (7) laser beaming UAV-to-CAEV, (8) laser beaming CAEV-to-UAV, (9) cabled charging, and (10) static wireless charging.

Table 1. Comparison of charging methods for CAEVs and UAV.

Method	Technology	Mobility	Main Benefit	Key Limitation
Wired Charging	Physical connectors	Stationary	High efficiency	Requires vehicle to stop
SWC	IPT/CPT	Stationary	Contactless automation	Requires precise alignment
DWC	Embedded IPT/Laser Beaming	In-motion	Charging while moving	Alignment sensitivity
V2V Charging	Wireless/Optical/Direct Link	Mobile	No fixed infrastructure needed	Coordination and safety challenges

2.2. State of the Art: DRL-Based Charging and Scheduling

Coordinating energy replenishment across heterogeneous and mobile agents requires adaptive and real-time decision-making. DRL [32–34] has emerged as a promising approach to meet this need, enabling vehicles to make dynamic charging and routing decisions under uncertainty, respond to congestion, and adapt to variable energy availability. This subsection reviews representative DRL-based approaches related to charging, scheduling, and energy-aware coordination, while also positioning closely related UAV trip-planning and AoI-driven studies to provide a complete view of the current research landscape.

Research on DRL for CAEVs has primarily focused on optimizing charging decisions, route planning, and station selection. For example, Ref. [35] formulates the Electric Vehicle Charging Routing Problem (EVCRP) as a graph and applies an Advantage Actor-Critic (A2C) algorithm to minimize travel cost based on location, State of Charge (SoC), and charging availability, achieving 11–27% reduction compared to classical approaches. Similarly, Ref. [36] introduces a constraint-based DRL method that improves scalability and reduces travel time by up to 30%, though it relies on pre-trained models and cannot adapt to real-time variations. A Proximal Policy Optimization (PPO)-based solution in [37] dynamically dispatches mobile charging stations to minimize delays, while Ref. [38] optimizes autonomous fleet dispatch under varying demand. These approaches, however, focus solely on ground vehicles, support only conventional plug-in or SWC (IPT, CPT) [5,21], and do not address coordination with aerial systems.

Recent CAEV-focused studies have further applied DRL to charging scheduling under operational and infrastructure constraints. Li et al. [39] investigated DRL-based charging scheduling for battery swapping stations to improve operational efficiency and quality of service under uncertainty. Rahali et al. [40] examined both model-based and model-free DRL approaches for EV smart charging, leveraging predictive control concepts to enhance constraint handling and adaptability to dynamic demand and renewable energy availability. Mousaei et al. [41] applied a DDPG-based control architecture to coordinate EV charging schedules with voltage regulation in distribution networks. While these works advance DRL-based charging control at individual stations or grid nodes, they focus on localized infrastructure and do not consider coordinated charging and trip planning across heterogeneous charging technologies or mixed CAEV–UAV transportation systems.

In the UAV domain, DRL has similarly been applied to flight trajectory optimization and mission-specific energy allocation, albeit under different mobility and energy constraints. Beyond energy-centric UAV scheduling, several studies have examined UAV trip planning and trajectory optimization for AoI-minimal data collection in UAV-assisted IoT networks. Zhu et al. [42] formulated AoI-minimal data collection as a generalized traveling salesman problem and optimized UAV visiting order and hovering locations. Liu et al. [43] studied long-term average AoI minimization in UAV-assisted wireless powered communication networks by jointly optimizing sensor transmission, clustering, and UAV trajectories. Zhang et al. [44] investigated AoI-aware data collection in pre-clustered UAV networks using learning-based coordination to balance information freshness and energy consumption. Liu et al. [45] addressed AoI-minimal task assignment and trajectory optimization

in multi-UAV-assisted IoT systems using clustering-based heuristic methods. While these works advance AoI-aware UAV routing and mission planning, they focus on UAV-centric IoT settings and do not address coordinated charging scheduling and energy management across mixed CAEV–UAV transportation systems.

Recent studies have further explored DRL for UAV charging and service scheduling under diverse operational assumptions. Huang et al. [46] proposed a decentralized A2C–Long Short-Term Memory (LSTM) framework for joint UAV service and charging scheduling under partial observability. Ma et al. [47] investigated multi-UAV charging coverage using an assisted DRL approach with survival incentives to balance user fairness and energy efficiency. Chen et al. [48] studied CUAV-assisted wireless charging and data acquisition, incorporating battery life prediction into DRL-based charging and scheduling decisions for both single- and multi-CUAV scenarios. While these works demonstrate the effectiveness of DRL for UAV-centric charging and scheduling, they remain limited to aerial platforms and do not consider coordinated charging across heterogeneous ground–aerial systems.

For instance, Ref. [49] jointly optimizes flight altitude, speed, and path radius to improve energy efficiency but does not consider interactions with ground vehicles or charging infrastructure. The Fair Charging–Trajectory Design Time Allocation (FC-TDTA) approach in [50] enhances throughput and fairness in Non-Orthogonal Multiple Access (NOMA) IoT networks but relies on offline training. A Deep Q-Network (DQN)-based solution in [51] improves UAV energy utilization during data collection but does not address fairness or free-rider issues. Meanwhile, a Partially Observable Markov Decision Process (POMDP)-based joint PPO (*j-PPO*) framework in [52] improves multi-UAV coordination but remains limited to aerial platforms, fixed infrastructure, and conventional or static wireless charging. Emerging technologies such as DWC, OWPT, and V2V charging introduce additional challenges not addressed by these works [22].

Across both domains, existing DRL approaches demonstrate promising results but share several limitations: most focus exclusively on either CAEVs or UAVs, rely on static infrastructure, and do not incorporate emerging charging methods or real-time operational conditions [12,18,22]. They also often lack mechanisms to handle uncertainties, such as early or late arrivals, fluctuating demand, or integrated payment and reservation validation [3,4,9]. These limitations directly motivate the three-layer architecture and progressively adaptive scheduling strategies introduced in this paper, which aim to integrate charging scheduling and trip planning within a unified decision-making framework aligned with the vision and requirements of emerging 6G-enabled ITS.

Building on these observations, the proposed SAFE-DDPG framework advances the state of the art by unifying ground and aerial charging coordination within a single scheduling framework, while explicitly supporting heterogeneous charging technologies such as DWC and V2V, uncertainty-aware decision-making, and integrated access validation mechanisms. Table 2 therefore presents a representative comparison of widely cited DRL-based charging and scheduling approaches, highlighting differences in focus, adaptability, and coordination scope, while complementary UAV trip-planning and charging studies are discussed in the text to contextualize the proposed contributions. Table 3 summarizes the gaps in existing works and demonstrates how SAFE-DDPG addresses critical challenges such as cross-domain coordination, diverse charging types, alignment handling, adaptive and event-driven operation , early and late arrival management, and integrated payment and secure access.

Table 2. Comparison of DRL-based charging and scheduling approaches.

Study	Primary Focus	Adapt.	Charging Support	Coord. Scope	Main Contribution
[35] A2C EVCRP	EV routing	S	P	G	Efficient route selection using SoC and charging availability
[36] Constraint-DRL	Path planning	L	P	G	Constraint-based planning decoupled from road topology
[37] PPO-MCS	Mobile charger dispatch	A	P	G	Dynamic dispatch of mobile chargers
[38] Autonomous fleet dispatch	Fleet dispatch	A	P	G	Fleet-level routing and charging optimization
[39] CAEV BSS DRL	Charging scheduling	A	P	G	DRL-based charging control for battery swapping stations
[40] EV smart charging	Charging scheduling	A	P	G	Model-based and model-free DRL for constrained EV charging
[41] Grid-aware EV DRL	Charging scheduling	A	P	G	DDPG-based charging coordination with grid constraints
[46] UAV serving/charging	UAV scheduling	A	W	A	Decentralized A2C–LSTM for UAV serving and charging under partial observability
[47] UAV charging coverage	UAV charging	A	W	A	Assisted DRL for multi-UAV charging coverage with fairness incentives
[48] CUAV-assisted UAV charging	UAV charging	A	W	A	DRL-based CUAV charging and scheduling with battery life prediction
[49] UAV mission optimization	UAV trajectory	P	W	A	Flight path and energy optimization for UAVs
[50] FC-TDTA	UAV path	A	W	A	Fairness-aware trajectory and energy scheduling
[51] DQN UAV	UAV energy management	A	W	A	Energy-aware UAV routing with queue management
[52] j-PPO ConvNTM	Multi-UAV coordination	C	W	A	Multi-UAV scheduling for improved resource allocation
SAFE-DDPG (This work)	**Integrated aerial–ground charging**	**A**	**P, W, D, V**	**A + G**	**Unified scheduling across platforms and charging technologies**

Keys: Adapt. (S = Static, L = Limited, A = Adaptive, P = Predefined, C = Context-aware); Charging (P = Plug-in, W = Wireless, D = DWC, V = V2V); Coord. (G = Ground, A = Aerial).

Table 3. System-level gaps addressed by existing approaches and this work.

Focus	[35]	[36]	[37]	[38]	[39]	[40]	[41]	[46]	[47]	[48]	[49]	[50]	[51]	[52]	**This Work**
Ground + aerial	–	–	–	–	–	–	–	–	–	–	–	–	–	–	**Yes**
Charging types	P	P	P	P	P	P	P	W	W	W	W	W	W	W	**M**
Alignment handling	–	–	–	–	–	–	–	–	–	–	L	L	L	L	**A**
Early & late arrivals	–	–	–	–	–	–	–	–	–	–	–	–	–	–	**Yes**
Real-time adaptability	–	–	Pa	Pa	Pa	Pa	Pa	Pa	Pa	Pa	–	L	Pa	C	**F**
Payment & access control	–	–	–	–	–	–	–	–	–	–	–	–	–	–	**Yes**

Keys: Charging (P = Plug-in, W = Wireless, M = Multiple); Adaptability (L = Limited, Pa = Partial, C = Context-aware, A = Adaptive, F = Full); Alignment handling (L = Limited or implicit consideration, A = Adaptive and explicitly modeled).

3. System Design and Architecture

3.1. System Overview

The proposed system integrates DWC for both CAEVs and UAVs, as illustrated in Figure 2. Within the UAV fleet, two specialized types are deployed: Laser-Beaming Uncrewed Aerial Vehicles (LBUAVs), equipped with larger batteries to provide in-flight charging to other UAVs and to CAEVs in emergency scenarios, and Edge Intelligent Uncrewed Aerial Vehicles (EIUAVs), which possess smaller batteries but offer critical edge intelligence services to CAEVs and act as mobile roadside units for 6G connectivity. LBUAVs schedule their charging routes to supply energy to EIUAVs through Laser Beaming (LB) without interrupting ongoing missions, effectively extending UAV operational times. Ground-based LB stations provide backup charging with higher energy capacity to UAVs when stationary.

On the ground, CAEVs benefit from multiple charging options including Cabled Charging Networks (CCNs), Static Wireless Charging Networks (SWCNs), Dynamic Wireless Charging Networks (DWCNs) embedded in roads, and CAEV-to-CAEV wireless charging. This diverse charging infrastructure ensures flexibility and continuous operation. The system includes a charging scheduling and trip planning IoT application tailored for ITS, coordinating UAV and CAEV energy demands and charging resources. This comprehensive framework enables efficient, real-time energy management across heterogeneous vehicle types, enhancing operational reliability and extending mission durations.

3.2. Proposed System Design and Architecture

Future 6G-enabled smart city environments, as envisioned by leading standardization bodies and industry consortia, including the 3rd Generation Partnership Project (3GPP) [53], International Telecommunication Union (ITU) [54], the Next Generation Mobile Networks (NGMN) Alliance [55], and recent industry white papers such as Ericsson's 6G spectrum report [56], are expected to fundamentally transform ITS. These efforts outline a vision for 6G that introduces advanced capabilities such as Ultra-Reliable Low-Latency Communication (URLLC), Massive Machine-Type Communications (mMTC), Integrated Sensing and Communication (ISAC), and Artificial Intelligence (AI). Collectively, these features are essential to enable data-intensive and time-critical mobility services, including coordinated charging, predictive route planning, and real-time energy orchestration for CAEVs and UAVs. Furthermore, 6G architectures emphasize semantic communication for context-aware data exchange, pervasive edge intelligence to support distributed decision-making, and advanced network slicing to meet diverse Quality of Service (QoS) demands across heterogeneous applications. A key enabler of this vision is Peer-to-Peer (P2P) connectivity among intelligent infrastructure elements, creating a fully connected backbone that supports low-latency coordination, scalable resource allocation, and seamless service delivery. These principles directly align with the objectives of our proposed system, which seeks to enable real-time coordination, interoperable charging operations, and autonomous decision-making within dense, dynamic ITS ecosystems.

Compared with monolithic or cloud-centric charging management architectures commonly adopted in existing systems, the proposed three-layer design explicitly separates time-critical control, local coordination, and global optimization. This separation is motivated by practical challenges observed in heterogeneous CAEV–UAV environments, including latency sensitivity, scalability limitations, and tight coupling between charging feasibility and scheduling decisions. Latency-critical functions such as alignment verification, arrival monitoring, and safety enforcement are handled at the end-device and edge layers, while the core cloud performs reservation arbitration, billing, and long-horizon optimization. By decoupling these functions, the architecture reduces signaling

overhead, limits dependence on centralized control during transient disruptions, and enables incremental deployment across heterogeneous charging networks and vehicle classes. In contrast to centralized or platform-specific solutions, this design provides a unified, practical, and deployable foundation for coordinated ground–aerial charging and scheduling, directly addressing the coordination, scalability, and real-time responsiveness challenges highlighted in Figure 1.

Building on these requirements, we propose a charging reservation and trip planning architecture tailored for 6G-enabled smart cities. The system employs a hybrid mesh-star network topology that enables efficient communication among Charging Network Managers (CNMs), which coordinate charging requests from both CAEVs and UAVs across multiple types of Charging Networks (CNs). Each CN type is managed by its dedicated CNM: the Cabled Charging Network Manager (CCNM) oversees all CCNs, the Static Wireless Charging Network Manager (SWCNM) manages all SWCNs, the Dynamic Wireless Charging Network Manager (DWCNM) controls all DWCNs, the Laser-Beaming Charging Network Manager (LBCNM) manages laser-beaming towers responsible for charging UAVs, the Aerial Vehicle Charging Network Manager (AVCNM) supervises all aerial vehicle charging networks, particularly managing all LBUAVs, and the Ground Vehicle Charging Network Manager (GVCNM) manages all Ground Vehicle Charging Networks (GVCNs) and directly handles all CAEVs.

Within this architecture, three complementary charging scheduling strategies are supported. SH-CSP provides a deterministic baseline using static system snapshots and predefined heuristics, enabling predictable operation under low dynamics. DH-CSP extends this approach by incorporating real-time state updates, allowing responsive adaptation to traffic, arrivals, and charging availability. SAFE-DDPG further generalizes scheduling by learning long-term policies under uncertainty, while explicitly enforcing feasibility and safety constraints through architecture-aware filtering. Together, these strategies form a hierarchical progression from rule-based control to adaptive learning, ensuring robustness across a wide range of operational conditions that are not simultaneously addressed by existing CAEV-only or UAV-only scheduling approaches.

As illustrated in Figure 3, P2P connectivity among these CNMs forms a fully connected backbone that supports UAV-to-CAEV and CAEV-to-UAV energy exchange, balanced load distribution, and seamless cross-network scheduling. AI-native orchestration is integrated into the proposed SAFE-DDPG algorithm and heuristic planning modules to autonomously optimize routing and resource allocation. Semantic communication within the handshake protocol enables efficient mission-critical data exchange, and network slicing ensures heterogeneous QoS requirements, such as millisecond-level latency for dynamic wireless charging and high-throughput links for laser-beaming operations, are satisfied. By leveraging these mechanisms alongside emerging 6G capabilities [10,11,54–56], the proposed architecture delivers a future-ready, interoperable platform for large-scale intelligent energy management in next-generation ITS.

The proposed system leverages a three-layer edge computing architecture to support efficient charging reservation and trip planning across heterogeneous networks. Computation and communication tasks are distributed among End Devices, Edge Intelligence Devices, and Core Cloud components to reduce latency, optimize processing, and enable real-time decision-making in line with 6G smart city requirements. This three-layer design is illustrated in Figures 4 and 5, with each figure depicting the architecture applied to different types of CNs and corresponding charging technologies.

1. End Devices: This layer consists of UAVs, CAEVs, and Electric Vehicle Supply Equipments (EVSEs). These devices initiate and relay charging requests, collab-

orating via Vehicle-to-Grid (V2G) and V2V communication protocols to facilitate energy transactions.

2. Edge Intelligence Devices: Located along roadways and in remote areas, this layer includes Roadside Units (RSUs), communication towers, and EIUAVs. While these devices may have higher latency than end devices, they significantly reduce the load on cloud servers by performing local data processing and computation offloading. They use Vehicle-to-Infrastructure (V2I) communication to improve network responsiveness and efficiency.
3. Core Cloud: This layer comprises Key Distribution Centers (KDCs), Banks, Energy Service Providers (ESPs), and Energy Distribution Centers (EDCs). The KDCs ensure secure communications through symmetric encryption, while the Bank facilitates transactions using Credit Points (CPs). The ESPs manage billing and energy distribution, and the EDCs coordinate charging reservations, route planning, and energy pricing.

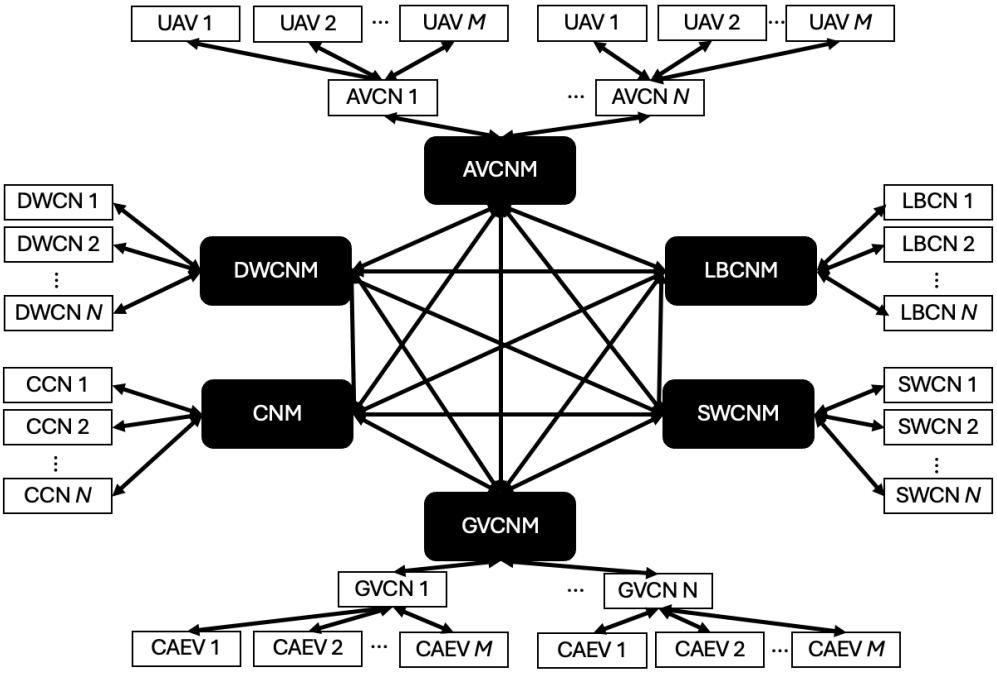


Figure 3. Communication topology of CNMs coordinating charging requests across heterogeneous networks including CCNM, SWCNM, DWCNM, AVCNM, and GVCNM.

Figure 4 illustrates the SWCN, highlighting inductive charging for stationary vehicles. The three-layer design facilitates precise alignment for energy transfer, local computation at edge intelligence devices, and cloud-level coordination for billing and reservation management.

While Figure 4 focuses on inductive charging for stationary vehicles, the same three-layer architecture also subsumes conventional CCN deployments as a special case. In CCNs, wired energy transfer replaces inductive coupling and alignment sensing, while reservation verification, authentication, queue management, and billing continue to operate across the end-device, edge intelligence, and core cloud layers. This abstraction illustrates that the proposed architecture is not tied to a specific charging technology, but instead provides a technology-agnostic coordination framework that can be incrementally deployed using existing infrastructure.

From an implementation perspective, separating latency-sensitive operations at the end-device and edge layers from global coordination in the cloud reduces system complexity and avoids monolithic controllers. This design supports practical deployment by

limiting real-time control loops to local components, while preserving interoperability and scalability across heterogeneous charging networks.

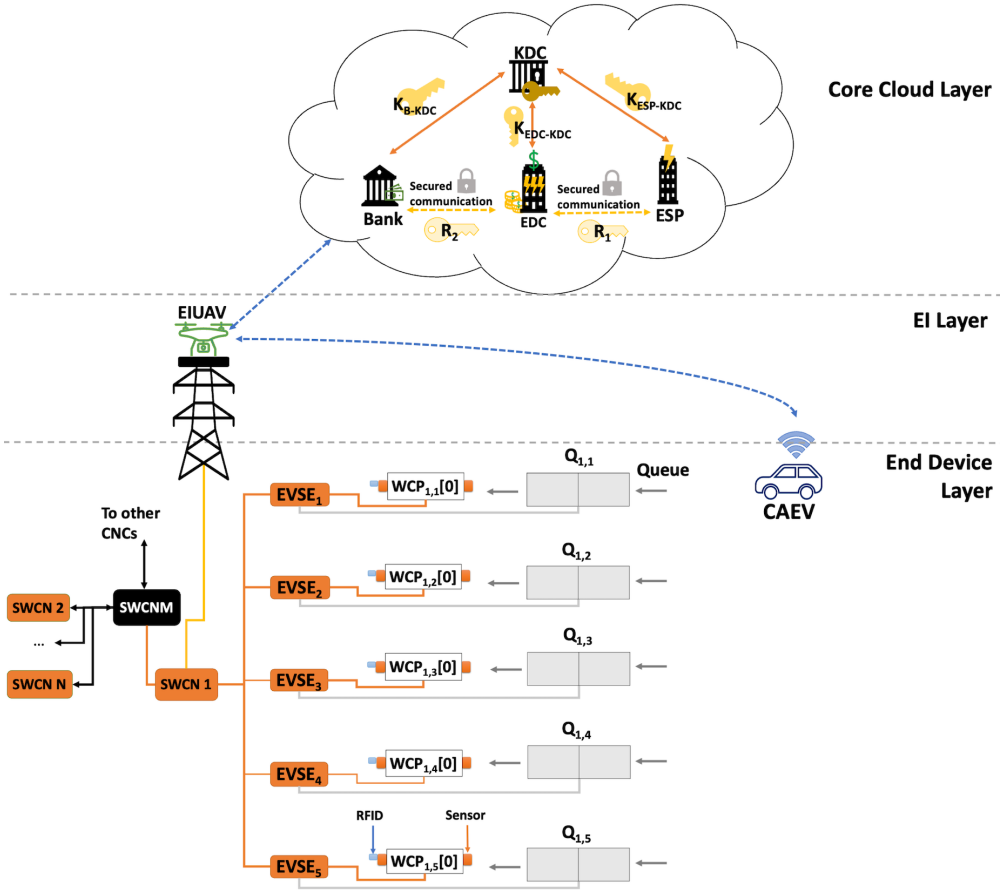


Figure 4. Three-layer architecture applied to the SWCN, highlighting inductive charging of stationary vehicles with distributed communication.

DWCNs follow the same architectural principles as the SWCN, with the primary difference that charging interfaces are distributed along roadway segments rather than concentrated at fixed locations. In this case, end-device and edge intelligence components monitor vehicle presence, alignment, and dwell time across successive charging segments, while CNMs coordinate segment availability and load distribution. Importantly, support for in-motion charging is achieved through localized coordination and scheduling, without requiring architectural modification or centralized real-time control, demonstrating that vehicle mobility can be accommodated within the same three-layer framework.

Figure 5 combines the Laser-Beaming Charging Network (LBCN), Aerial Vehicle Charging Network (AVCN), and GVCN. This configuration demonstrates advanced charging technologies, including laser beaming, UAV-to-CAEV coordination, and distributed cross-network energy sharing. It is supported by edge intelligence and core cloud orchestration.

Figure 5 demonstrates how the proposed architecture extends naturally to heterogeneous ground–aerial environments, enabling coordinated operation across LBCN, AVCN, and GVCN. Unlike platform-specific or centralized solutions, cross-network coordination is achieved through standardized interfaces and distributed edge intelligence, allowing UAVs and CAEVs to participate in reservation, scheduling, and energy exchange without bespoke control logic.

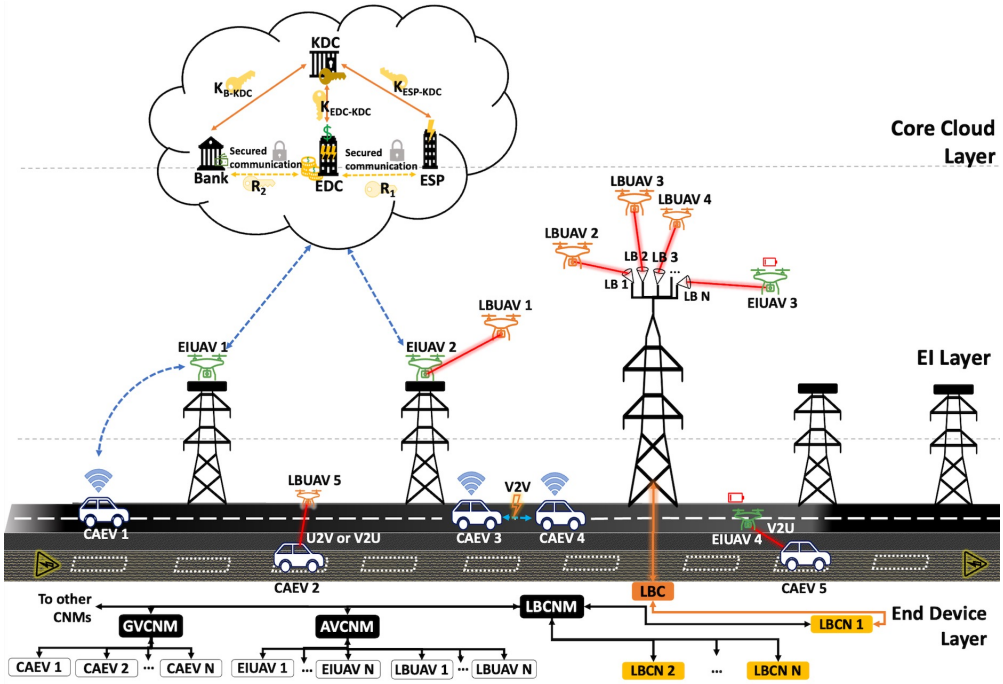


Figure 5. Three-layer architecture for the LBCN, AVCN, and GVCN, demonstrating advanced charging technologies and distributed cross-network coordination between UAVs and CAEVs.

This separation between physical charging mechanisms and coordination logic supports incremental deployment, where new vehicle classes or charging technologies can be integrated without redesigning the system. As a result, the architecture offers a scalable and deployment-feasible foundation for future 6G-enabled ITS, distinguishing it from existing solutions that remain tightly coupled to individual platforms or charging modalities.

This multi-tiered architecture reduces latency and optimizes computational efficiency by processing data closer to the source, improving responsiveness for both UAVs and CAEVs acting as edge servers. By minimizing unnecessary cloud communication, it lowers network traffic, reduces operational costs, and conserves energy, which is particularly important for UAVs with limited battery capacity. Integrating 6G and IoT technologies, the system provides low-latency communication, real-time data exchange, and flexible charging management across diverse vehicle types. Support for various charging methods, including laser beaming, enhances the system's adaptability and sustainability in future smart city mobility frameworks.

Overall, the architecture enables intelligent and scalable management of extensive charging demands across interconnected networks and leverages emerging 6G capabilities to enhance energy efficiency and operational performance for next-generation ITS.

3.3. Handshake Protocol

The proposed system introduces a comprehensive charging scheduling and trip planning protocol designed to support both CAEVs and UAVs. This protocol enables secure, efficient, and dynamically optimized charging sessions while coordinating trip planning within smart city infrastructures. Key components of the scheduling and planning protocol include the following:

1. Initiating Charging Requests and Trip Plans:
    (a) Requesting Process: Both CAEVs and UAVs initiate charging requests based on their current SoC, location, and intended destinations. CAEVs can send requests directly or forward them to nearby EIUAVs. LBUAVs relay their own or other UAVs charging requests to EIUAVs, which act as local coordinators

managing and aggregating requests. The system supports CAEVs-to-CAEVs and CAEVs-to-UAVs charging interactions as well.

(b) Anonymity and Tracking: To protect user privacy, EIUAVs add randomized identifiers to charging and trip requests, enabling secure tracking without compromising operator anonymity.

2. Optimizing Charging Scheduling and Trip Planning:

   (a) Coordination with CNMs: EIUAVs communicate with CNMs to evaluate charging station availability, vehicle chargers, or DWCs options along routes for both CAEVs and UAVs.

   (b) Dynamic Route and Schedule Optimization: The system calculates optimized routes and charging schedules based on energy needs, infrastructure availability, traffic or aerial congestion, and operational constraints. Reservation details and trip plans are sent to CAEVs and UAVs to ensure timely and conflict-free charging with minimal delays.

3. Establishing and Managing Charging Sessions:

   (a) Authentication and Confirmation: CAEVs and UAVs receive reservation confirmations including charging times, locations, and secure authentication credentials.

   (b) Energy Transfer and Safety: Vehicles can be charged using various methods, including cabled charging, static and dynamic wireless charging, laser power transfer, or V2V energy exchange. Continuous communication ensures proper alignment, safety, and efficiency.

4. Real-Time Monitoring, Payment, and Adaptation:

   (a) Session Monitoring: Energy consumption and charging progress are monitored in real time for accuracy and operational oversight.

   (b) Secure Payment: Billing supports two main models: pay-per-energy-unit, where users pay based on the kilowatt-hours delivered during the session, and pay-per-charging-session, where billing occurs at the end of the session. Both models utilize encrypted virtual currencies (CP) to ensure secure transactions. Dynamic pricing mechanisms can be applied to reflect varying electricity costs or network load.

   (c) Adaptive Scheduling: The system dynamically updates charging schedules and trip plans in response to real-time changes such as delays or infrastructure availability, thus maintaining seamless operations.

   These real-time updates affect system-level scheduling decisions by enabling reservation reassignment, timing adjustments, and charging handover within the proposed three-layer architecture. Runtime adaptation is event-driven and executed using pre-trained policies and deterministic heuristic rules, such that bounded reaction time is determined by monitoring, control signaling and payment authorization, and execution or enforcement at the charging infrastructure.

   From a theoretical perspective, all deployment-time operations follow a bounded control flow with finite message exchanges and fixed computational complexity. Heuristic schedulers evaluate a finite set of candidate charging options, while the learning-based scheduler performs a single forward pass of a pre-trained policy network. No iterative optimization, convergence process, or online retraining is required during operation. As a result, real-time performance is governed by bounded communication overhead and constant-time decision execution, enabling predictable and deployment-feasible responses to delays, misalignment, and infrastructure availability changes, consistent with the low-latency and edge-assisted operation assumed in 6G-enabled ITS.

This integrated charging scheduling and trip planning protocol supports coordinated and efficient operation of CAEVs and UAVs within 6G-enabled smart city environments. It facilitates sustainable energy management alongside optimized mobility. Figure 6 summarizes the end-to-end interaction among vehicles, edge coordinators, and charging infrastructure, illustrating how reservation verification, alignment validation, and billing are integrated into a single operational loop rather than treated as independent processes.

Figure 6 depicts the process by which a CAEV verifies its charging reservation upon arrival at the designated charging network. After receiving its scheduled charging reservation and trip plan, the CAEV communicates with a nearby coordinator, such as an EIUAV, to confirm the reservation. The coordinator interacts with the corresponding charging network manager to verify the reservation and to activate the appropriate charging components, including the EVSE and, when applicable, the wireless charging platform.

Sensors and Radio-Frequency Identification (RFID) can be used to enable accurate vehicle identification and positioning, while communication technologies such as Light Fidelity (Li-Fi), Wi-Fi, or 6G can be accommodated to provide real-time feedback and alignment verification for precise and safe charging. This flexible system supports a variety of communication technologies to adapt to different operational environments. The system performs authentication and safety checks to guarantee secure access to the charging infrastructure. During the charging process, energy delivery and session status are continuously reported to the energy data center, enabling real-time monitoring and accounting.

Billing is managed with metered payments based on energy consumed or session duration, and dynamic pricing mechanisms can be applied to optimize charging costs. As illustrated in Figure 6, billing can be performed incrementally on a per-energy-unit basis or finalized at the end of the charging session. The session is automatically terminated when vehicle departure or misalignment is detected, triggering power shutoff and final settlement.

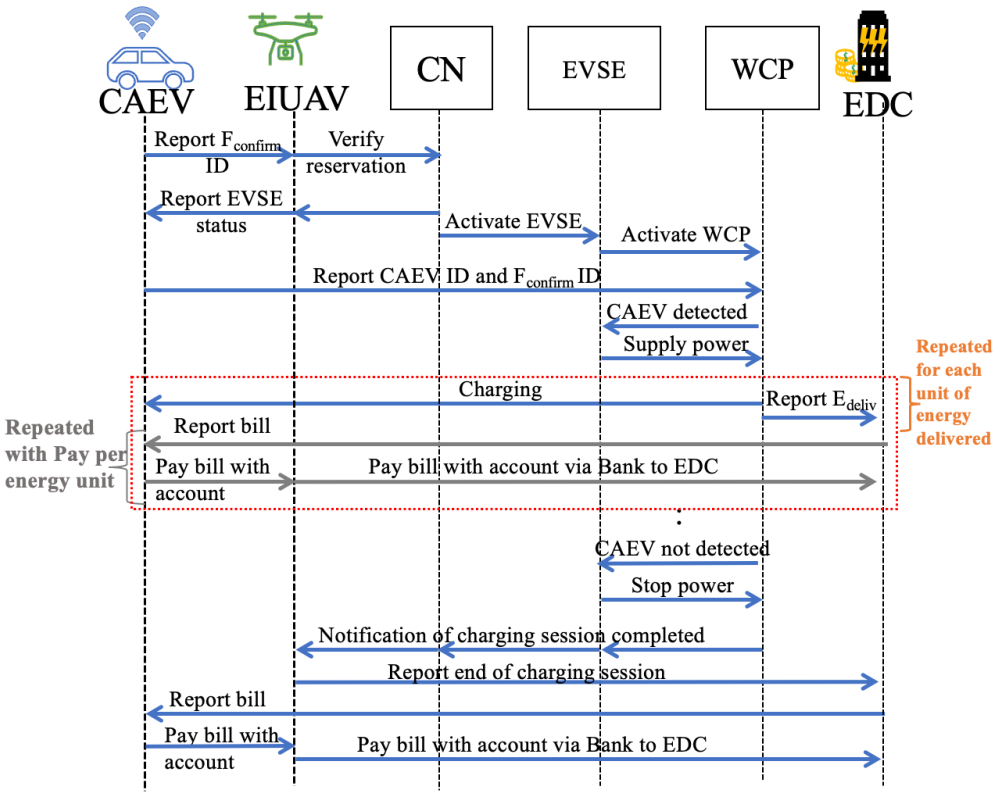


Figure 6. End-to-end handshake process for a CAEV charging session, illustrating reservation verification, charging activation, real-time monitoring, and billing settlement using the proposed protocol.

3.4. Modeling and Algorithms

3.4.1. Power Consumption Models for UAVs and CAEVs

The rotary-wing UAV power consumption model captures the essential aerodynamic and mechanical characteristics of multi-rotor drones, grounded in well-established single-rotor physics [57,58]. This foundation allows consistent extension to multi-rotor UAVs [59,60], accommodating various designs while preserving physical realism and enabling accurate estimation of energy requirements for flight and charging operations.

The UAV propulsion power model accounts for hover, cruise, and vertical motion based on established rotary-wing aerodynamics. For clarity and conciseness, the detailed derivation of the individual hover, horizontal-flight, and vertical-motion power components is provided in Appendix A. Here, we focus on the resulting compact mobility-aware propulsion power expression used in scheduling and charging decisions.

The total power consumption for steady three-dimensional flight with horizontal velocity V_h and vertical velocity V_v is given by the following:

$$P_{total}(V_h, V_v) = P_{mhov} + \Delta P_h(V_h) + \Delta P_v(V_v) \tag{1}$$

where $\Delta P_h(V_h)$ represents the velocity-dependent parasitic and induced power components for horizontal motion, and $\Delta P_v(V_v)$ represents the vertical velocity-dependent aerodynamic and induced power components for ascent and descent, as derived in Appendix A.

This formulation captures hover, horizontal flight, vertical ascent and descent, and combined 3D maneuvers, maintaining a compact and physically interpretable power equation. It incorporates essential physical and aerodynamic parameters to provide a realistic and computationally efficient estimation of UAV power consumption during critical maneuvers. This adaptability enables precise trajectory optimization and energy management, supporting enhanced flight endurance across diverse UAV platforms and environmental conditions.

The power consumption of CAEVs is modeled using a component-level physics-based approach [61], capturing drivetrain, battery, and vehicle dynamics. The total wheel force F_W acting on the vehicle is modeled as shown in (2), which accounts for gravitational force on a slope, rolling resistance, aerodynamic drag, and the inertial effects of acceleration. Here, m is the vehicle mass, g the gravitational acceleration, α the road slope angle, f_r the rolling resistance coefficient, ρ the air density, c_w the aerodynamic drag coefficient, A_f the frontal area, v the velocity, a the acceleration, and e_i the equivalent inertia factor representing rotating components.

$$F_W = mg\sin\alpha + mgf_r\cos\alpha + \frac{1}{2}\rho c_w A_f v^2 + me_i a \tag{2}$$

The wheel torque T_W is derived by multiplying the total wheel force by the wheel radius r_W, as expressed in (3).

$$T_W = F_W \cdot r_W \tag{3}$$

This wheel torque is then converted to the motor shaft torque T_{EM} by accounting for the gear ratio i_T and transmission efficiency η_T, as described in the piecewise function in (4). The case distinction allows proper handling of driving and regenerative braking torques.

$$T_{EM} = \begin{cases} T_W \cdot i_T^{-1} \cdot \eta_T^{-1}, & T_W \geq 0, \\ \max\left(T_W \cdot i_T^{-1} \cdot \eta_T, T_{W,min}\right), & T_W < 0, \end{cases} \tag{4}$$

The motor power loss map $P_{EM,loss}$ is modeled as a nonlinear function of motor speed n_{EM} and torque T_{EM}:

$$P_{EM,loss} = f(n_{EM}, T_{EM}) \tag{5}$$

This function captures the efficiency characteristics of the electric motor more accurately than constant-efficiency assumptions.

Finally, battery power consumption $P_{Bat,chem}$ is computed using the nonlinear relationship given in (6), which models battery voltage U_0 and internal resistance R_i, and relates electrical motor power $P_{EM,el}$ and auxiliary power $P_{aux,el}$ to actual battery chemical power consumption.

$$P_{Bat,chem} = \frac{U_0^2}{2R_i} - \frac{U_0}{2R_i}\sqrt{U_0^2 - 4R_i(P_{EM,el} + P_{aux,el})} \tag{6}$$

Compared to simplistic energy models that often rely on constant coefficients or aggregated power estimates, detailed component-level modeling of CAEV power consumption provides more precise and physically realistic energy estimates. This level of detail is essential for capturing vehicle behavior under varying traffic conditions and operational scenarios, and for evaluating wireless charging strategies effectively.

The CAEV power model complements the UAV propulsion model by providing a physically grounded representation of traction power demand under realistic driving conditions. Together, these models enable consistent estimation of energy consumption across ground and aerial vehicles, forming the basis for mobility-aware charging feasibility, arrival-time prediction, and coordinated scheduling decisions.

Beyond power modeling, UAV mobility is explicitly formulated to capture how vehicle motion influences scheduling and charging decisions. The mobility of UAVs is formulated using a continuous three-dimensional kinematic model with bounded velocity, acceleration, and altitude constraints, consistent with commonly adopted rotary-wing UAV mobility and propulsion models in the literature [57–60]. The model captures hovering, cruising, ascent, and descent behaviors, and directly links UAV motion to propulsion energy consumption and mission timing.

The impact of the mobility model on the proposed strategies is reflected through its coupling with residual energy, arrival time at charging points, alignment duration, and charging feasibility. Variations in UAV movement dynamically influence scheduling states and constraint satisfaction, thereby affecting reservation decisions, charging handovers, and priority assignment. As a result, both heuristic and learning-based schedulers operate on mobility-aware system states rather than abstract trajectories, ensuring that scheduling and charging decisions remain valid under realistic UAV motion dynamics.

3.4.2. Charging Communication Model

Laser beaming is an emerging and highly efficient method for DWC of both CAEVs and UAVs. In the proposed system, high-power laser beams are used for energy transfer, while lower-power beams enable optical communication based on Li-Fi principles with On–Off Keying (OOK) modulation [24,62,63]. Laser-beaming charging nodes can be fixed infrastructure, such as LBCNs, or mobile platforms, including CAEVs and UAVs, and may serve as transmitters delivering optical energy to receivers mounted on UAVs or other CAEVs. This facilitates in-motion energy transfer across multiple configurations, including CAEVs–UAVs, UAVs–UAVs, CAEVs–CAEVs, and LBCN–UAVs. The same optical links also support high-speed Line-of-Sight (LOS) communication, with laser power dynamically allocated between charging and communication according to operational priorities.

The received optical charging power, P_{LRec} is modeled in (7) as follows:

$$P_{LRec} = \eta_{LRec}\, P_{LTrans}\, \frac{A_{LRec}}{d_L^2}\, LOS\, Env_\lambda \tag{7}$$

where η_{LRec} is the optical-to-electrical conversion efficiency of the receiver, P_{LTrans} is the laser transmitter power (W), A_{LRec} is the effective aperture area of the receiver (m^2), d_L is the transmitter–receiver separation (m), $LOS \in [0,1]$ accounts for geometric LOS, and $Env_\lambda \in [0,1]$ represents wavelength-dependent atmospheric attenuation.

The average optical communication power for OOK modulation is expressed in (8) as follows

$$P_{comm} = \eta_{CTrans}\, \frac{E_b}{T_b}\, \frac{A_{CRec}}{d_C^2}\, LOS\, Env_\lambda \tag{8}$$

where η_{CTrans} is the optical communication transmission efficiency, E_b is the energy per bit (J), T_b is the bit duration (s), A_{CRec} is the communication receiver aperture area (m^2), and d_C is the communication link distance (m). The term $\frac{E_b}{T_b}$ represents the average transmission power per bit.

The critical charging distance d_{crit} is obtained by inverting (7) for d_L when $P_{LRec} = P_{\min}$, the minimum power required by the receiver for sustained charging, yielding the following (9):

$$d_{crit} = \sqrt{\frac{\eta_{LRec}\, P_{LTrans}\, A_{LRec}\, LOS\, Env_\lambda}{P_{\min}}} \tag{9}$$

where $P_{\min}$ is in watts. This applies equally to CAEV–UAV, UAV–UAV, CAEV–CAEV, and LBCN–UAV charging links.

Similarly, the critical communication distance d_{comm} is obtained by inverting (8) for d_C when $P_{comm} = P_{req}$, the minimum received power required for reliable decoding, as shown in (10).

$$d_{comm} = \sqrt{\frac{\eta_{CTrans}\, E_b\, A_{CRec}\, LOS\, Env_\lambda}{T_b\, P_{req}}} \tag{10}$$

Finally, the optimal alignment angle θ between transmitter and receiver for maximum charging efficiency is given in (11):

$$\theta = arccos\left(\frac{P_{LRec}}{P_{LMax}}\right) \tag{11}$$

where P_{LMax} is the maximum allowable received optical power (W). This factor accounts for geometric beam alignment and ensures that the optical link operates within safe power limits while maintaining maximum energy transfer efficiency, regardless of whether the source is an LBCN tower, a CAEV, or another UAV.

Equations (7)–(11) provide a unified, dimensionally consistent framework for modeling joint charging and communication in mixed CAEV–UAV networks, UAV–UAV swarms, and infrastructure-supported operations. This approach is realistic because it incorporates physical optical link parameters, atmospheric attenuation, and receiver conversion efficiency, which are validated in free-space optical communication and wireless power transfer literature. Furthermore, its parametric form allows adaptation to different hardware specifications, environmental conditions, and operational priorities, enabling accurate link budgeting and deployment planning in real-world scenarios.

3.4.3. Battery Management and Charging Model

To support coordinated charging of both CAEVs and UAVs, the system assumes a linear two-stage battery model [64] that provides a practical and physically grounded

representation of lithium-ion battery behavior. Unlike simplified formulations that assume perfect adherence to pilot signals, this model captures the charging process through two distinct phases: bulk and absorption. During the bulk phase, typically from 0% to 70–90% SoC, the charging current remains nearly constant, while in the absorption phase, the current decreases linearly as the battery voltage stabilizes.

The charging rate at time t, $\widehat{r}(t)$, is defined in (12) as follows:

$$\widehat{r}(t) = min\{r(t), \bar{r}, \widehat{e}(t)\} \tag{12}$$

where $r(t)$ is the pilot signal charging rate, $\bar{r}$ is the maximum charging rate allowed by the charger, and $\widehat{e}(t)$ is the remaining battery capacity at time t. This rate is further refined using a piecewise linear approach to reflect the different charging phases, as given in the following (13):

$$\widehat{r}(t) = \begin{cases} min\{r(t), \bar{r}, \widehat{e}(t)\}, & \text{if SoC} \leq th \\ \min\left\{\left(1 - \frac{\text{SoC}-th}{1-th}\right) r_1, r(t)\right\}, & \text{otherwise} \end{cases} \tag{13}$$

where SoC is the state-of-charge, th is the threshold separating the bulk and absorption phases, and r_1 is the charging rate at the start of absorption. This formulation accurately reflects the tapering of current as the battery approaches full charge, as illustrated in Figure 7, which compares the linear two-stage model with an idealized model and shows the realistic decline in current during the absorption phase. Importantly, this model applies regardless of the charging technology, whether wired, Magnetic Resonance (MR) wireless charging, or laser beam power transfer, since the battery management system ultimately governs charging current and voltage profiles. Environmental and charger-specific factors can be incorporated by adjusting $r(t)$ or $\bar{r}$, enhancing realism.The linear two-stage model provides a reliable and computationally efficient basis for energy management, supporting coordinated charging and optimized operational performance for heterogeneous fleets of CAEVs and UAVs.

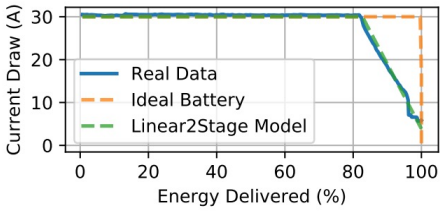


Figure 7. Comparison of the linear two-stage battery charging model [64] with an idealized model, demonstrating realistic tapering of charging current as the battery approaches full state-of-charge.

Although real-world battery charging can exhibit nonlinear behavior due to temperature, C-rate, and aging effects, the adopted two-stage model is intentionally selected to balance physical realism and computational efficiency. Temperature- and charger-dependent efficiency variations can be incorporated through bounded charging rates $r(t)$ and $\bar{r}$. Importantly, the proposed scheduling and learning framework is agnostic to the specific battery model and remains applicable under more complex nonlinear formulations, which can be integrated without modifying the coordination architecture or SAFE-DDPG training procedure.

3.4.4. Charging Scheduling and Trip Planning

The charging scheduling and trip planning algorithm is designed for both CAEVs and UAVs within a three-layer hierarchical architecture. The process begins when a vehicle sends its current SoC, the requested SoC, vehicle type, trip start location, and trip

destination to the nearest EIUAV or RSU. This node generates a reservation request frame containing these parameters and forwards it to the EDC, which processes the request and relays it to the ESP. If two vehicles request charging simultaneously, priority is given to the one with the lower current SoC.

At the ESP, candidate CNs are first filtered based on geographic proximity, availability within the vehicle's predicted arrival–departure time window and charging cost. Candidate vehicles for V2V DWC are also identified according to distance, availability, and ability to supply energy to the requesting vehicle. The requested charging amount is then distributed between dynamic CNs types (DWCN, AVCN, GVCN) and static CNs types (SWCN, LBCN, CCN). CAEVs exclude LBCN from consideration, whereas UAVs exclude CCN, SWCN, and DWCN. Operational thresholds for each CN type are configurable parameters.

Each CN is evaluated using a dynamic weighted score, shown in (14), where c_i is the charging cost at CN i (monetary units), t_i is the estimated travel time to CN i (s), w_i is the waiting time at CN i (s), b_i is the battery energy consumption to reach CN i (Wh), d_i is the travel distance to CN i (m), and λ_1 through λ_5 are adaptive weight coefficients:

$$\text{score} = \lambda_1 c_i + \lambda_2 t_i + \lambda_3 w_i + \lambda_4 b_i + \lambda_5 d_i \tag{14}$$

The trigger condition for initiating charging is improved in (15) to unify both at-CN and in-transit triggers:

$$\text{ChargeReq}_i = \begin{cases} 1, & SoC_i < SoC_{req} \text{ at CN} \\ 1, & SoC_i < SoC_{th} \text{ in transit} \\ 0, & \text{otherwise} \end{cases} \tag{15}$$

Here, $\text{ChargeReq}_i = 1$ indicates a charging request for vehicle i is triggered, SoC_{req} is the mission-required charge level at a CN, and SoC_{th} is the emergency threshold in transit.

Reservation timing is ensured by (16), where t_{arr_i} is the predicted arrival time at CN i, t_{res_i} is the reservation start time, and t_{dep_i} is the predicted departure time:

$$t_{arr_i} \leq t_{res_i} \leq t_{dep_i} \tag{16}$$

Travel distance constraints between consecutive CNs are enforced in (17) , where $d(i,j)$ is the travel distance between CN i and CN j, and $D_{\max}$ is the maximum allowable distance:

$$d(i,j) \leq D_{\max} \tag{17}$$

Energy sufficiency is checked using (18), where E_{rem} is the remaining stored energy after the last charging event, E_{cons_i} is the energy consumed over segment i, $\mathcal{N}$ is the set of segments before the next charging event, and $E_{\min}$ is the minimum operational reserve:

$$E_{rem} - \sum_{i \in \mathcal{N}} E_{cons_i} \geq E_{\min} \tag{18}$$

Finally, charging efficiency is verified via (19), where η_i is the measured efficiency at CN i and $\eta_{\min}$ is the minimum acceptable efficiency:

$$\eta_i \geq \eta_{\min} \tag{19}$$

Following CN scoring and constraint verification, the CNM searches for available EVSEs that meet the requirements, and the ESP chooses the optimal one according to priority rules. For CAEVs, the order from least to most priority is CCN, SWCN, GVCN, AVCN, and DWCN, excluding LBCN. For UAVs, the order is LBCN, AVCN, GVCN, excluding

CCN, SWCN, and DWCN. When scores tie, the CN with the shortest travel distance is selected. Once dynamic and, if needed, static CNs are reserved, the Reservation Confirmation Frame is issued with a unique anonymized identifier to enable secure verification while preserving privacy.

Routing is then performed online to follow the reserved CN locations. For UAVs, trip routing is handled by a three-dimensional A* algorithm, as expressed in (20), where $f(n)$ is the total estimated path cost through node n, $g(n)$ is the accumulated cost from the start node to n, $h(n)$ is the heuristic estimate from n to the goal, $c_{alt}(n)$ is the altitude-related energy cost, and $c_{obs}(n)$ is the obstacle-avoidance cost:

$$f(n) = g(n) + h(n) + c_{alt}(n) + c_{obs}(n) \tag{20}$$

CAEV routing is performed online using Dijkstra's algorithm [65]. The minimal cumulative travel cost $D(v)$ to reach node v from source s is calculated according to (21), where $\text{Pred}(v)$ denotes the set of predecessor nodes to v and $c(u, v)$ is the travel cost between nodes u and v:

$$D(v) = \min_{u \in \text{Pred}(v)} \{D(u) + c(u, v)\} \tag{21}$$

The proposed Algorithms 1 and 2 systematically schedule wireless charging for both CAEVs and UAVs by prioritizing requests, filtering candidate charging networks, and optimizing routing based on vehicle type and real-time conditions. This approach ensures efficient charging reservations and dynamic trip planning, enhancing overall energy management and operational reliability in heterogeneous vehicular networks.

Algorithm 1 Charging scheduling for CAEVs and UAVs.

Input: SoC_i, SoC_{req}, SoC_{th}, veh_{type}, $start_{loc}$, $dest_{loc}$
Output: Reserved dynamic CNs (optional static CNs), Reservation Confirmation ID
BEGIN

1. Send reservation request frame from nearest EIUAV/RSU to EDC.
   1.1. Include SoC_i, SoC_{req}, veh_{type}, $start_{loc}$, and $dest_{loc}$.
2. Forward processed request from EDC to ESP.
3. **IF** multiple simultaneous requests **THEN**
   3.1. Assign priority to vehicle with lower SoC_i.
4. Filter candidate CNs at ESP by:
   4.1. Geographic proximity to $start_{loc}$.
   4.2. Availability within predicted arrival and departure window.
   4.3. Charging cost.
5. Identify candidate vehicles for V2V DWC based on distance, availability, and compatibility.
6. Distribute requested charging amount among CNs:
   6.1. Dynamic CNs: DWCN, AVCN, GVCN.
   6.2. Static CNs: SWCN, LBCN, CCN.
   6.3. **IF** veh_{type} = CAEV **THEN** exclude LBCN.
   6.4. **IF** veh_{type} = UAV **THEN** exclude CCN, SWCN, DWCN.
7. **FOR EACH** candidate CN **DO**
   7.1. Compute score (14).
   7.2. Verify constraints (16)–(19).
8. Select optimal dynamic CN by veh_{type} priority.
9. **IF** scores tie **THEN** select CN with minimum d_i.
10. Reserve selected dynamic CN.
11. **IF** additional charging required **THEN**
    11.1. Reserve optimal static CN using same procedure.
12. Generate reservation confirmation frame with anonymized ID.
13. Return reservation details to vehicle.

END

Algorithm 2 Online trip routing following charging reservation.

Input: Reserved CNs locations, veh_{type}, traffic/flight data
Output: Optimal route to CNs and final destination
BEGIN
1: Receive confirmed CNs locations from **Algorithm 1**.
2: **if** veh_{type} = UAV **then**
3: Use (20)
4: **end if**
5: **if** veh_{type} = CAEV **then**
6: Use (21)
7: **end if**
8: Generate initial route from current location to reserved CN.
9: **while** en route **do**
10: Monitor traffic conditions (CAEVs).
11: Monitor flight obstacles and altitude costs (UAVs).
12: **if** major delay or blockage detected **then**
13: Recalculate route to CN using same algorithm.
14: **end if**
15: **end while**
16: **Upon arrival at CN:**
17: **IF** additional CN reserved **THEN**
18: Repeat Steps 8–16 for next CN.
19: After final charging, route to destination.
END

3.4.5. Charging Alignment and Correction for CAEVs and UAVs

Pre-Charging Operational Constraints

After reservation, authentication, and verification between the CAEV or UAV and the EVSE, the charging mode identifier contained in the CN message determines the operational constraints for that session. The selected wireless charging type may be static or dynamic. Magnetic Resonance Wireless Power Transfer (MR-WPT), which can operate in SWC, DWC, or V2V configurations between vehicles of the same or different types, or Laser Beaming Wireless Power Transfer (LB-WPT), which may occur between a LBCN tower and a UAV, or between two vehicles in a V2V configuration.

Before wireless power is delivered, the EVSE verifies that the vehicle's speed, relative angle, separation distance, and orientation meet the requirements of the chosen charging mode. These requirements are defined in (22)–(38) and are specific to the selected technology. Continuous monitoring of these parameters is performed during the charging process. If any parameter deviates from its permissible bounds such as lateral misalignment in SWC or DWC, excessive beam misalignment in LB-WPT, or coupling distance variation in MR-WPT, then charging is immediately halted for safety. Power transfer resumes automatically once all monitored parameters are restored to their acceptable ranges, thereby maintaining operational safety and sustained energy transfer efficiency.

Mode-Specific Geometric and Kinematic Requirements

In SWC, the CAEV must remain stationary with minimal misalignment between the receiver coil center and the wireless charging pad center. Let $v_{a,SWC}$ be the actual vehicle speed, $\Delta x_{SWC} = X_{c,SWC} - x_{a,SWC}$ and $\Delta y_{SWC} = Y_{c,SWC} - y_{a,SWC}$ be the longitudinal and lateral offsets between the pad center $(X_{c,SWC}, Y_{c,SWC})$ and the actual receiver coil center $(x_{a,SWC}, y_{a,SWC})$. The tolerances $\epsilon_{x,SWC}$ and $\epsilon_{y,SWC}$ define the allowable misalignment. The SWC condition is expressed in (22):

$$v_{a,SWC} = 0, \quad |\Delta x_{SWC}| \leq \epsilon_{x,SWC}, \quad |\Delta y_{SWC}| \leq \epsilon_{y,SWC} \tag{22}$$

Society of Automotive Engineers (SAE) J2954 recommends $\epsilon_{y,SWC}$ within ±75–100 mm laterally and negligible longitudinal motion for efficient coupling [66].

For DWC, the CAEV is in motion. Let $v_{t,DWC}$ be the target speed, $\delta_{v,DWC}$ the speed tolerance, and $\epsilon_{y,DWC}$ the lateral misalignment tolerance. The vehicle must satisfy the following (23):

$$|v_{a,DWC} - v_{t,DWC}| \leq \delta_{v,DWC}, \quad |\Delta y_{DWC}| \leq \epsilon_{y,DWC} \tag{23}$$

Field experiments from narrow-width IPT and high-power dynamic Wireless Power Transfer (WPT) systems indicate $\delta_{v,DWC} \approx 0.3$ m/s and $\epsilon_{y,DWC} \approx 0.10$ m for high transfer efficiency [67,68].

In LB-WPT for V2V charging between same or different vehicle types, both platforms must be stationary relative to each other, and UAVs must hover. For LBCN tower delivery to a UAV, the UAV must hover. Let $\epsilon_{x,LB}$ and $\epsilon_{y,LB}$ be the allowable offsets, d_{LB} the separation between laser transmitter and receiver apertures, and $d_{\min,LB}$, $d_{\max,LB}$ the minimum and maximum safe distances. The constraints are given in the following (24):

$$\begin{gathered} v_{a,LB} = 0, \quad |\Delta x_{LB}| \leq \epsilon_{x,LB}, \quad |\Delta y_{LB}| \leq \epsilon_{y,LB}, \\ d_{\min,LB} \leq d_{LB} \leq d_{\max,LB} \end{gathered} \tag{24}$$

Recent LB-WPT UAV charging tests report $d_{\min,LB} = 10$ m, $d_{\max,LB} = 500$ m, and lateral offsets $\epsilon_{x,LB} = \epsilon_{y,LB} = 0.05$ m in controlled safe zones [63]. These may be adjusted to comply with national laser safety regulations.

In MR-WPT V2V operation, vehicles may be stationary or moving, provided relative speed and coupling distance remain within limits. Let $d_{a,MR}$ be the measured coil distance, $d_{t,MR}$ the optimal resonant distance, $\delta_{d,MR}$ the allowable distance deviation, and $\delta_{v,MR}$ the speed tolerance. The requirement is given in the following (25) :

$$|v_{a,MR} - v_{t,MR}| \leq \delta_{v,MR}, \quad |d_{a,MR} - d_{t,MR}| \leq \delta_{d,MR} \tag{25}$$

Strongly coupled MR-WPT results suggest $\delta_{d,MR}$ should be maintained within $\pm 7\%$ of coil diameter for optimal coupling efficiency [69].

Speed correction in any moving mode k where $k \in \{DWC, MR\}$ is governed by (26)–(28). Let $r_{v,k}$ be the mode-specific acceleration or deceleration rate:

$$|v_{a,k} - v_{t,k}| \leq \delta_{v,k} \tag{26}$$

$$v_{a,k} \leftarrow v_{a,k} + r_{v,k} \quad \text{if} \quad v_{a,k} < v_{t,k} - \delta_{v,k} \tag{27}$$

$$v_{a,k} \leftarrow v_{a,k} - r_{v,k} \quad \text{if} \quad v_{a,k} > v_{t,k} + \delta_{v,k} \tag{28}$$

A rate $r_{v,k} \approx 0.005$ m/s per ms (5.0 m/s^2) matches measured acceleration profiles from high-power DWC/MR-WPT trials [68], balancing fast convergence and passenger comfort.

The pad center coordinates $(X_{c,k}, Y_{c,k})$ are given in the following (29):

$$X_{c,k} = \frac{X_{s,k} + X_{e,k}}{2}, \quad Y_{c,k} = \frac{Y_{s,k} + Y_{e,k}}{2} \tag{29}$$

Misalignment correction proceeds until (30) is met:

$$|\Delta x_k| \leq \epsilon_{x,k}, \quad |\Delta y_k| \leq \epsilon_{y,k} \tag{30}$$

For MR-WPT or LB-WPT V2V, the gap constraint (31) applies, with positions updated by–along unit vector $\mathbf{u}_k$:

$$|d_{a,k} - d_{t,k}| \leq \delta_{d,k} \tag{31}$$

$$\mathbf{p}_{1,k} \leftarrow \mathbf{p}_{1,k} + \frac{(d_{a,k} - d_{t,k})}{2}\mathbf{u}_k \tag{32}$$

$$\mathbf{p}_{2,k} \leftarrow \mathbf{p}_{2,k} - \frac{(d_{a,k} - d_{t,k})}{2}\mathbf{u}_k \tag{33}$$

Power Transfer Modeling for LB-WPT

In LB-WPT, the received power $P_{r,LB}$ is given in (34):

$$P_{r,LB} = P_{t,LB} \cdot \eta_{sys,LB} \cdot \left(\frac{D_{r,LB}}{D_{b0,LB} + \theta_{LB} \cdot d_{LB}}\right)^2 \tag{34}$$

The maximum distance meeting required power $P_{req,LB}$ is computed from (35):

$$d_{LB} = \frac{\sqrt{\frac{P_{t,LB} \cdot \eta_{sys,LB} \cdot D_{r,LB}^2}{P_{req,LB}}} - D_{b0,LB}}{\theta_{LB}} \tag{35}$$

subject to (36):

$$d_{\min,LB} \leq d_{LB} \leq d_{\max,LB}, \quad P_{r,LB} \geq P_{req,LB} \tag{36}$$

The optimal beam elevation angle $\alpha_{opt,LB}$ is defined in (37):

$$\alpha_{opt,LB} = \underset{\alpha \in \mathcal{A}_{LB}}{argmax}\ P_{r,LB}(d_{LB}(\alpha)) \tag{37}$$

To account for UAV hovering and CAEV vibration, a jitter attenuation term $\eta_{jitter,LB}$ is applied as in (38):

$$\eta_{jitter,LB} = e^{-\frac{\sigma_{jitter,LB}^2}{2\sigma_{beam,LB}^2}} \tag{38}$$

where $\sigma_{jitter,LB}$ is the standard deviation of pointing error and $\sigma_{beam,LB}$ is the beam spot size at the receiver. This has been validated in controlled laser charging trials [63].

The following Algorithm 3 formalizes the complete process of monitoring, detecting, and correcting positional, speed, and beam-alignment deviations to ensure optimal conditions for safe and efficient wireless power transfer across all supported vehicles, charging types and technologies.

Algorithm 3 Charging alignment and correction for CAEVs and UAVs

Input: Vehicle type $T \in \{CAEV, UAV\}$,
charging mode $k \in \{SWC, DWC, LB, MR\}$,
target parameters $v_{t,k}$, $\epsilon_{x,k}$, $\epsilon_{y,k}$, $\delta_{v,k}$, $\delta_{d,k}$, $d_{t,k}$, $d_{\min,k}$, $d_{\max,k}$, $\alpha_{\text{opt},k}$
Output: Charging status (ON/OFF), updated position and speed
Begin
Receive reservation, authentication, and CN message from EVSE
Identify vehicle type T
Determine charging mode k based on T and CN
while session_active **do**
  Measure $v_{a,k}$, Δx_k, Δy_k, $d_{a,k}$, orientation, and beam angle (if LB)
  if any constraint from (22)–(25) is violated **then**
    Charging ← OFF
    if $k \in \{DWC, MR\}$ **then**
      Correct speed using (26)–(28)
    end if
    if positional or distance misalignment present **then**
      For SWC or DWC, correct lateral/longitudinal offset using (29)–(30)
      For MR or LB V2V, correct gap using (31)–(33)
    end if
  else
    if $k = LB$ **then**
      Compute $P_{r,LB}$ using (34)
      Verify range and power conditions in (36)
      Adjust beam angle via (37)
      Apply jitter attenuation from (38)
    end if
    Charging ← ON
  end if
end while
End

3.4.6. Dynamic Arrival Handling

The proposed charging coordination framework addresses both early and late arrivals for CAEVs and UAVs operating in infrastructure-based DWC and ad-hoc DWC modes. By leveraging real-time communication, predictive arrival time estimation, and adaptive scheduling, the system minimizes wasted capacity, reduces waiting time, and ensures efficient utilization of charging resources.

Vehicle arrival times are estimated using real-time traffic and flight data, route calculations, and environmental conditions. For CAEVs, the arrival time $t_{arr,CAEV}$ is predicted using the following (39):

$$t_{arr,CAEV} = t_{current} + \frac{d_{CAEV}}{v_{CAEV}} + \Delta t_{traffic} + \Delta t_{queue} \tag{39}$$

where $t_{current}$ is the system clock time, d_{CAEV} is the road distance to the CN entry point, v_{CAEV} is the predicted travel speed based on real-time traffic and routing data, $\Delta t_{traffic}$ is the estimated traffic delay, and Δt_{queue} is the expected waiting time before entering the CN. Equation (39) ensures that both route-dependent and congestion-related delays are accounted for in scheduling decisions.

Similarly, UAV arrival time $t_{arr,UAV}$ is computed as in the following:

$$t_{arr,UAV} = t_{current} + \frac{d_{UAV}}{v_{UAV}} + \Delta t_{wind} + \Delta t_{queue} \tag{40}$$

where d_{UAV} is the straight-line distance to the CN, v_{UAV} is the cruise velocity, Δt_{wind} is the delay or gain due to wind speed and direction, and Δt_{queue} represents waiting time if the reserved EVSE is occupied. Equation (40) allows UAV scheduling to reflect real atmospheric conditions, improving arrival accuracy.

Early Arrival Handling

For infrastructure-based DWC, a CAEV arriving before its scheduled time may enter the track immediately if the number of vehicles currently charging $n_{track}(t)$ is below the allowable maximum $n_{\max}$, as expressed in the following (41):

$$n_{track}(t) < n_{\max} \tag{41}$$

where $n_{\max}$ is set to maintain safe throughput and charging efficiency. If condition (42) is not satisfied, the CAEV is routed along a parallel road until entry is possible.

Reservation updates for early arrivals occur when a currently charging CAEV is expected to vacate the lane within a time window Δt_{update}, as given in the following (42):

$$t_{free} - t_{current} \leq \Delta t_{update} \tag{42}$$

where t_{free} is the estimated departure time of the next vehicle. When (42) holds, the arriving CAEV's booking is updated, and its previous slot is released for reallocation.

For UAVs, if an EVSE is available upon arrival, charging begins immediately. If not, the UAV joins the queue and the queue length is updated as $q_{\text{len}} \leftarrow q_{\text{len}} + 1$.

If $q_{len} > q_{\max}$, the UAV must choose between waiting in a nearby holding position or cancelling and rebooking at an alternative location. This choice is represented in the following (43):

$$tatus_i = \begin{cases} \text{Wait}, & \text{if space available} \\ \text{Rebook}, & \text{if space unavailable} \end{cases} \tag{43}$$

In ad-hoc DWC, synchronization between the Charge Delivery Vehicle (CDV) and Charge Receiving Vehicle (CRV) is crucial. Successful rendezvous requires satisfying (44):

$$|t_{arr,CDV} - t_{arr,CRV}| \leq \Delta t_{sync} \tag{44}$$

where Δt_{sync} is the allowable time offset for initiating charging. If (44) is violated, the system may reschedule or reassign pairings to maintain efficiency.

Late Arrival Handling

For infrastructure-based DWC, late-arriving CAEVs may still enter the track if traffic flow constraints allow. Otherwise, they are rescheduled for the next available slot. If partial missed time can be recovered, the system extends the departure time $t_{dep,CAEV}$ to (45):

$$t_{dep,CAEV'} = t_{dep,CAEV} + \Delta t_{late} \tag{45}$$

where Δt_{late} is the additional time required to meet the original charging requirement. If no extension is available, the CAEV is routed to a secondary charging site.

For UAVs, the same approach applies, with departure time updated using the following (46):

$$t_{dep,UAV'} = t_{dep,UAV} + \Delta t_{late} \tag{46}$$

In ad-hoc DWC, if the CDV is late, the CRV may be reassigned to a different delivery vehicle or given the option to wait or rebook. If the CRV is late, the CDV is reassigned when possible.

Henceforth, the algorithms are referred to as the SH-CSP approach, which employs fixed scheduling without dynamic arrival handling, and the DH-CSP approach, which incorporates dynamic arrival handling, for clear distinction throughout this work.

Algorithm 4 summarizes the logic for handling early and late arrivals for CAEVs and UAVs.

3.4.7. Proposed DRL Algorithm

Efficient scheduling and trip planning for CAEVs in smart city networks requires low-latency, reliable decision-making. Various DRL algorithms offer different trade-offs in sample efficiency, policy determinism, and computational overhead. A comparative evaluation guides the selection of the most suitable approach for large-scale, real-time coordination.

Deployment-Oriented Selection of DDPG for CAEV Online Scheduling

Several DRL algorithms were evaluated for real-time CAEVs charging scheduling and trip planning, including PPO [70], Soft Actor-Critic (SAC) [71], Twin Delayed Deep Deterministic Policy Gradient (TD3) [72], and DDPG [73]. The selection of DDPG as the base algorithm is driven primarily by deployment-time requirements rather than training-phase performance alone. In the proposed system, scheduling decisions are triggered by discrete events such as vehicle arrivals, misalignment detection, or reservation updates, and must be executed with bounded latency at edge or near-edge nodes. DDPG employs deterministic policy outputs and requires a single forward pass of the actor network per decision at inference time, enabling predictable, safety-compliant decision-making in hybrid and continuous action spaces with low computational latency and high sample efficiency.

In contrast, stochastic policy methods such as PPO [70] and SAC [71] introduce variability in action outputs and typically require larger volumes of newly collected data to stabilize, making them less suitable for safety-constrained, event-driven scheduling. TD3 [72], while effective in improving training stability through enhanced value estimation, incurs additional computational overhead due to its dual-critic architecture and policy smoothing

mechanisms, increasing per-decision complexity at inference time. These training-phase advantages do not translate into proportional gains for event-triggered online charging scheduling with frequent policy re-evaluation, where deterministic execution and bounded inference latency at deployment are the dominant constraints. The proposed SAFE-DDPG framework relies on deterministic actor outputs that can be externally post-processed and feasibility-checked during training to stabilize learning, a design that aligns naturally with DDPG's deterministic policy gradient formulation but is less compatible with inherently stochastic policies or multi-critic architectures.

Algorithm 4 Dynamic arrival handling for CAEVs and UAVs

Input: Vehicle type $T \in \{CAEV, UAV\}$
Mode $\in$ {Infrastructure-*DWC*, Ad-hoc-*DWC*}
Arrival time t_{arr}
Reservation info
Output: Charging action
Begin
if EarlyArrival **then**
  if Mode == Infrastructure-DWC **then**
    if T == CAEV (DWCN) **then**
      if (41) holds **OR** (42) holds **then**
        Start charging immediately
      else
        Wait in parallel lane or rebook
      end if
    else if T == UAV (LBCN) **then**
      if EVSE available **then**
        Start charging
      else if queue length $< q_{\max}$ **then**
        Join queue
      else
        Wait or rebook (43)
      end if
    end if
  else if Mode == Ad-hoc-DWC **then**
    if (44) holds **then**
      Rendezvous charging
    else
      Wait, reassign, or rebook
    end if
  end if
end if
if LateArrival **then**
  if Mode == Infrastructure-DWC **then**
    if T == CAEV (DWCN) **then**
      Resume charging; extend if possible (45)
    Else rebook or go to secondary site
    else if T == UAV (LBCN) **then**
      Resume charging; extend if possible (46)
    Else rebook or go to secondary site
    end if
  else if Mode == Ad-hoc-DWC **then**
    Reassign pairing, wait, or rebook
  end if
end if
End

Accordingly, a deployment-oriented screening based on deterministic execution, inference complexity, and compatibility with safety-aware integration was used to guide the algorithm selection process, as summarized in Table 4.

Table 4. Deployment-oriented comparison of candidate DRL algorithms for real-time CAEV charging scheduling.

Feature/Requirement	PPO [70]	SAC [71]	TD3 [72]	DDPG [73]	SAFE-DDPG (Proposed)
Policy Type at Inference	Stochastic	Stochastic	Deterministic	Deterministic	**Deterministic**
Sample Efficiency (Training)	Low	Moderate	High	High	**High**
Computational Efficiency	Low	Low	Moderate	High	**High**
Inference-Time Networks Required	Actor + Critic	Actor + Critic	Actor + Dual Critics	Actor only	**Actor only**
Forward Passes per Decision	2	2	3	1	**1**
Latency Suitability	Moderate	Low	Moderate	High	**High**
Handles Continuous Actions	Yes	Yes	Yes	Yes	**Yes**
Training-Time Feasibility Enforcement	No	No	No	No	**Yes**
Sequential Per-Vehicle Control	No	No	No	No	**Yes**
Adaptive Exploration	Limited	Entropy-based	Limited	OU noise (fixed)	**OU noise (adaptive)**
Domain Alignment	Low	Low	Medium	Medium	**High**

While Table 4 captures the deployment-oriented screening criteria that motivated selecting DDPG as the baseline, the subsequent simulation section examines the performance impact of the additional safety, feasibility, and coordination mechanisms introduced in SAFE-DDPG under identical network and traffic conditions.

SAFE-DDPG: Safety-, Scheduling-, and Sustainability-Aware Feasibility-Enhanced DDPG

Baseline DDPG Formulation

The DDPG algorithm employs an actor–critic architecture for continuous action control. The critic network $Q(\mathbf{s}_t, \mathbf{a}_t; \theta^Q)$, parameterized by θ^Q, minimizes the temporal-difference (TD) error:

$$L(\theta^Q) = \mathbb{E}\left[\left(y_t - Q(\mathbf{s}_t, \mathbf{a}_t; \theta^Q)\right)^2\right] \tag{47}$$

where the target y_t is computed as follows:

$$y_t = r_t + \gamma Q'\left(\mathbf{s}_{t+1}, \mu'(\mathbf{s}_{t+1}; \theta^{\mu'}); \theta^{Q'}\right) \tag{48}$$

γ is the discount factor, and primed networks (Q', μ') are target copies updated by the following:

$$\theta' \leftarrow \tau\theta + (1-\tau)\theta', \quad \tau \ll 1 \tag{49}$$

The actor $\mu(\mathbf{s}_t; \theta^\mu)$, parameterized by θ^μ, updates its policy via the deterministic policy gradient as follows:

$$\nabla_{\theta^\mu} J \approx \mathbb{E}_{\mathbf{s}_t}\left[\nabla_{\mathbf{a}} Q(\mathbf{s}_t, \mathbf{a}; \theta^Q)|_{\mathbf{a}=\mu(\mathbf{s}_t)} \nabla_{\theta^\mu} \mu(\mathbf{s}_t; \theta^\mu)\right] \tag{50}$$

While effective in generic domains, vanilla DDPG lacks safety constraints, fairness objectives, and adaptive exploration features essential for real-time CAEV scheduling.

State–Action Representation for Heterogeneous Charging Networks

The state vector in the implemented SAFE-DDPG framework extends beyond the original heterogeneous charging network specification by incorporating both vehicle-centric and environment-centric features relevant to real-time scheduling. At decision step t, the state vector is defined as follows:

$$
\begin{aligned}
s_t = [&SoC_{curr},\ SoC_{req},\\
&D_{dest},\ D_{static_\min},\ D_{dynamic_\min},\\
&\rho_{CAEV},\ \rho_{UAV},\\
&L_{CCN1},\ L_{CCN2},\ L_{SWCN1},\ L_{SWCN2},\\
&L_{DWCN1},\ L_{DWCN2},\ L_{AVCN1},\ L_{GVCN1},\\
&n_{sched},\ n_{wait},\\
&\tau_{sim},\ \tau_{elapsed},\ \eta_{last}]^T
\end{aligned}
\tag{51}
$$

Here, SoC_{curr} and SoC_{req} represent the normalized current and requested SoC of the CAEV. D_{dest} denotes the normalized route distance to the trip destination, while $D_{static_\min}$ and $D_{dynamic_\min}$ are the normalized minimum distances to the nearest static CN and dynamic CN, respectively. ρ_{CAEV} and ρ_{UAV} are density measures capturing the proximity and concentration of surrounding agents.L_i terms represent the normalized utilization levels of charging nodes. The variables n_{sched} and n_{wait} denote the normalized numbers of scheduled and currently waiting vehicles, respectively. τ_{dec} is the normalized decision time index, τ_{int} is the normalized decision interval, and η_{last} represents the proportion of static charging energy in the previous decision.

The continuous action vector a_t in this implementation consists of four components: a normalized index for selecting a dynamic CN, a normalized index for selecting a static CN,and the target SoC values for each. These continuous outputs are mapped to discrete CN assignments and feasible SoC targets during decision execution, enabling joint optimization of location choice and charging level.These continuous indices are post-processed into discrete charging node selections and admissible SoC targets, enabling simultaneous optimization of location choice and charging level within the heterogeneous CN.

Feasibility-Aware Action Filtering with DH-CSP Fallback

Every actor-generated action $\mathbf{a}_t^{\text{DRL}}$ is evaluated by the feasibility function $\mathcal{F}(\mathbf{s}_t, \mathbf{a}_t)$, which enforces SoC reachability, CN capacity, booking constraints, and route feasibility. This ensures that the vehicle can physically reach the selected charging node under the current operational conditions. If $\mathcal{F} = 0$, indicating an infeasible action, it is replaced by the heuristic output $\mathbf{a}_t^{\text{heuristic}}$ generated by the DH-CSP module:

$$
\mathbf{a}_t^{final} = \begin{cases} \mathbf{a}_t^{heuristic}, & \mathcal{F} = 0 \\ \mathbf{a}_t^{DRL}, & \text{otherwise.} \end{cases}
\tag{52}
$$

The fallback policy is not learned or imitated by the actor and is progressively eliminated through explicit penalization as training converges. This feasibility-aware filtering layer prevents unsafe or infeasible actions from being executed during early learning while ensuring that the replay buffer is populated with constructive experiences, which improves training stability and convergence efficiency compared to vanilla DDPG. The feasibility filter and heuristic fallback are primarily employed during training. As learning progresses, the actor internalizes feasibility constraints through consistent feedback from the filtered environment, resulting in a converged policy that rarely triggers fallback actions. During deployment, the learned policy operates in a fully deterministic, actor-only inference mode, with the feasibility check retained solely as a fail-safe to guarantee operational safety under unforeseen conditions.

Dual-Stage Reward

The local reward encourages immediate operational efficiency while penalizing imbalance, excessive routing overhead, and infeasible decisions:

$$R_t = -\frac{\left(SoC_{req} - \widehat{SoC}\right)^2}{SoC_{req} + \epsilon} - \beta_1 L_{dyn} - \beta_2 \frac{d_{dyn}}{d_{\max}} - \beta_3 L_{stat} - \beta_4 \frac{d_{stat}}{d_{\max}} + B_{lowLoad} - P_{fallback} - P_{feasibility} \quad (53)$$

where $\widehat{SoC}$ is the predicted post-charge SoC, L_{dyn} and L_{stat} are load imbalance metrics, d_{dyn} and d_{stat} are travel distances, $B_{lowLoad}$ rewards use of underloaded CNs, $P_{fallback}$ penalizes heuristic reliance, and $P_{\text{feasibility}}$ penalizes infeasible CN selections. This design ensures that selected CNs meet SoC requirements, avoid overloaded CNs, and remain reachable within operational constraints.

The global reward, applied after each episode, enforces long-term fairness and sustainability, and is adaptively scaled to match the magnitude of immediate rewards. It is defined as follows:

$$R_{\text{global}} = w_{\text{util}} U_{\text{CN}} - w_{\text{wait}} W_{\text{avg}} - w_{\text{idle}} I_{\text{avg}} - w_{\text{travel}} C_{\text{travel}} - w_{\text{batt}} C_{\text{batt}} - P_{\text{fallback}} \quad (54)$$

where U_{CN} is the mean CN utilization across CNs, W_{avg} is the average normalized wait time, I_{avg} is the average normalized idle time, C_{travel} is the normalized travel cost, C_{batt} is the normalized battery consumption cost, and P_{fallback} is a nonlinear penalty that increases with the fallback usage frequency. The final reward is scaled by a factor proportional to the mean absolute value of immediate rewards in the episode.

By combining utilization maximization with penalties for waiting time, idle capacity, travel, battery consumption, and fallback reliance, this reward structure incentivizes policies that maintain high network efficiency while avoiding congestion, unnecessary travel, and over-reliance on heuristics. The adaptive scaling ensures that the global reward remains balanced with immediate rewards, preventing one objective from dominating the learning process and encouraging stable, long-term improvements in system performance.

Neural Architecture and Action Selection

The SAFE-DDPG agent adopts a deep actor–critic design optimized for stability, precision, and real-time operation in dynamic charging environments. Both networks employ progressively reduced fully connected layers to efficiently extract relevant features, with carefully chosen activation functions, initialization, and normalization promoting smooth gradient flow and convergence under non-stationary demand. Regularization and dropout improve robustness to noise and variability without hindering learning. The critic network fuses state and action inputs early to enhance value estimation, while the actor produces bounded continuous actions that naturally map to admissible control ranges, eliminating the need for manual clipping. Additional stability is achieved through online reward normalization, gradient clipping, and delayed training onset to ensure representative minibatches. Finally, continuous outputs are post-processed into discrete charging-node selections and target SoC levels that are compatible with heterogeneous network constraints. Collectively, these design choices enable SAFE-DDPG to converge reliably with low latency and high decision quality, providing a robust solution for adaptive charging in heterogeneous network conditions.

Stabilized Prioritized Experience Replay

In the proposed framework, the standard experience replay mechanism in vanilla DDPG is replaced with a stabilized Prioritized Experience Replay (PER) strategy to improve

convergence speed and training stability in dynamic charging network environments. The sampling probability of each stored transition is defined as follows:

$$P(i) = \frac{(|\delta_i| + \epsilon)^{\alpha}}{\sum_j (|\delta_j| + \epsilon)^{\alpha}} \tag{55}$$

where δ_i denotes the Temporal Difference (TD) error, ϵ avoids zero probabilities, and α controls the degree of prioritization. The associated importance-sampling weights are computed as follows:

$$w_i = \left(\frac{1}{N} \cdot \frac{1}{P(i)} \right)^{\beta} \tag{56}$$

with β gradually annealed during training to correct sampling bias as learning progresses. For numerical stability, all w_i values are normalized by dividing them by the maximum weight before being applied in gradient updates.

To further enhance stability, newly observed transitions are optimistically assigned the current maximum priority, ensuring they are rapidly integrated into the learning process. TD-error updates are smoothed through a weighted blending of previous and current priorities to mitigate sudden fluctuations, and rewards are normalized before storage to prevent large magnitudes from dominating updates. These refinements collectively accelerate convergence and improve robustness under dynamic arrival patterns and heterogeneous charging network conditions compared to standard replay mechanisms.

Adaptive Ornstein–Uhlenbeck Exploration Noise

To further improve policy exploration, an adaptive Ornstein–Uhlenbeck (OU) process for action noise is introduced. In contrast to vanilla DDPG, which employs fixed-variance OU noise, the noise variance σ_t in SAFE-DDPG evolves according to the following:

$$\sigma_t = max(\sigma_{\min}, \sigma_0 \cdot \text{decay}^t) \tag{57}$$

This gradual decay ensures that large exploratory deviations dominate early in training, when policy uncertainty is high, while a moderate level of stochasticity is preserved in later stages to allow continual adaptation to changing system conditions.

Through the combination of stabilized PER and adaptive OU noise, SAFE-DDPG achieves superior learning stability, adaptability, and convergence speed compared to vanilla DDPG, particularly in highly dynamic, safety-critical scheduling environments.

Training Algorithm

The training process for SAFE-DDPG, summarized in Algorithm 5, is designed for online, sequential scheduling in heterogeneous charging networks. At each step, the actor network produces a deterministic continuous action (dynamic CN index, static CN index, target SoCs) perturbed by adaptive OU noise (57) for exploration. Actions are evaluated by a feasibility filter (52) that enforces SoC reachability and CN capacity constraints, with infeasible actions replaced by a DH-CSP heuristic fallback to ensure safety and operational continuity. Local rewards are computed immediately (53), and transitions are stored in a PER (55)–(56). After each episode, a global reward is calculated (54) to reflect fairness, network utilization, wait times, and fallback usage, and distributed across the stored transitions. The actor and critic networks are updated from mini-batches sampled from the buffer using DDPG loss functions (47)–(50), with target networks softly updated (49) for stability. This procedure enables the agent to balance short-term efficiency with long-term objectives while maintaining safety and robustness in dynamic, non-stationary charging networks.

Algorithm 5 SAFE-DDPG training with feasibility filtering and dual-stage rewards

Begin
procedure TRAINSAFE-DDPG
  Initialize actor $\mu(\cdot|\theta^{\mu})$, critic $Q(\cdot|\theta^{Q})$, and target networks μ', Q'
  Initialize PER buffer $\mathcal{D}$, noise parameters σ_0, $\sigma_{\min}$, decay rate
  for each episode **do**
    Observe initial environment state
    for each timestep t **do**
      for each vehicle v in active set **do**
        $\mathbf{s}_t^v \leftarrow$ vehicle-specific state from (51)
        $\mathbf{a}_t^v \leftarrow \mu(\mathbf{s}_t^v|\theta^{\mu}) + \text{OU_Noise}(\sigma_t)$ ▷ per (57) adaptive OU noise
        if $\mathcal{F}(\mathbf{s}_t^v, \mathbf{a}_t^v) = 0$ per (52) **then**
          $\mathbf{a}_t^v \leftarrow$ heuristic decision (DH-CSP fallback)
        end if
        Execute $\mathbf{a}_t^v$, observe R_t^v per (53), $\mathbf{s}_{t+1}^v$
        Store $(\mathbf{s}_t^v, \mathbf{a}_t^v, R_t^v, \mathbf{s}_{t+1}^v)$ in $\mathcal{D}$ with PER (55)–(56)
      end for
      Sample mini-batch from $\mathcal{D}$, update Q via (47)–(48), μ via (50)
      Soft-update targets μ', Q' via (49)
      $\sigma_t \leftarrow \max(\sigma_{\min}, \sigma_t \times \text{decay})$ per (57)
    end for
    Compute R_{global} per (54)
    Distribute R_{global} to episode transitions
  end for
end procedure
End

Overall, SAFE-DDPG extends the standard DDPG framework into a feasibility-aware, stability-focused, and efficiency-optimized Reinforcement Learning (RL) agent for heterogeneous charging networks. Its state–action representation integrates operational, temporal, and feasibility features to support policies that generalize across diverse network layouts and demand patterns. Safety and feasibility are enforced through action screening and heuristic fallback mechanisms, while learning stability is enhanced by normalized rewards, PER, gradient constraints, and regularized network design. Adaptive exploration ensures effective policy search early in training and precise control as the policy matures. Collectively, these design choices enable SAFE-DDPG to learn robust, high-quality policies that balance short-term efficiency with long-term objectives, providing a reliable framework for real-time vehicle scheduling in dynamic, safety-critical environments.

4. Simulation and Results

4.1. Setup

We simulate the proposed three-layer architecture and handshake protocol using the SH-CSP, DH-CSP, and SAFE-DDPG algorithms. For benchmarking, we also implement the vanilla DDPG algorithm to compare against our SAFE-DDPG approach.

A discrete-time event simulator was developed to model the integrated operation of CAEVs and UAVs under various charging systems and control strategies. The simulator was executed for a continuous two-day horizon, from 5 June 2025 to 6 June 2025, and Ontario's TOU pricing is applied [74,75].

Vehicle mobility and routing for CAEVs were modeled using the Simulation of Urban MObility (SUMO) platform [76,77] to ensure realistic traffic and path-planning behavior. UAVs were custom modeled within the simulator to incorporate heterogeneous charging systems and energy consumption profiles. The simulation included 50 CAEVs, 8 LBUAVs, and 6 EIUAVs, each modeled using a linear two-stage battery model. CAEV parameters

were derived from the EV Database [78] to ensure realistic energy consumption, range, and charging characteristics, while UAV parameters are summarized in Table 5.

Table 5. Summary of UAV Parameters.

Parameter	LBUAV	EIUAV	Parameter	LBUAV	EIUAV
W (N)	39.2	6.9	LOS (–)	0.9	0.9
n (–)	4	4	Env_λ (–)	0.95	0.95
r (m)	0.20	0.13	P_{LTrans} (W)	1000	–
A (m^2)	0.1257	0.0531	A_{LRec} (m^2)	0.088	0.037
C_T (–)	0.095	0.095	$\text{SF}P_{\parallel}$ (m^2)	0.20	0.12
ρ (kg/m^3)	1.225	1.225	V_v^{asc} (m/s)	3.0	1.5
δ_s (–)	0.05	0.05	V_v^{desc} (m/s)	−2.5	−1.5
k (–)	0.5	0.5	$\text{SF}P_{\perp}$ (m^2)	0.20	0.12
V_h (m/s)	15.0	10.0	v_0 (m/s)	6.32	4.42

The UAV parameters in Table 5 were selected to ensure realistic flight dynamics, energy consumption, and operational capabilities. LBUAVs are larger and heavier than EIUAVs, with higher weight, rotor size, and rotor area, providing the lift and stability required for both flight and wireless charging missions. Both UAV types use four rotors to balance maneuverability with power efficiency. Lift and drag characteristics were chosen based on standard rotorcraft aerodynamics to accurately model hovering and vertical motion, while body size, air density, and flat-plate areas account for environmental effects and aerodynamic drag during horizontal and vertical flight [59,60]. Operational velocities, including horizontal speeds and vertical ascent/descent rates, were set to balance energy efficiency, safety, and mission timing. LOS and environmental factors reflect communication and sensing constraints in urban conditions. The transmitter power for LBUAVs ensures sufficient energy transfer for wirelessly charging other UAVs. These parameter choices enable the power consumption models to simulate hovering, horizontal, vertical, and combined 3D maneuvers accurately, supporting trajectory planning, energy management, and integration with heterogeneous charging networks.

For simulation purposes, LBUAVs employ 6S LiPo batteries, while EIUAVs use 3S LiPo batteries. The CAEV road network is generated using a large-scale synthetic SUMO environment with a wide aggregate spatial extent corresponding to the cumulative length of modeled road segments, intended to emulate spatially distributed routing and charging demand rather than a single continuous operational area. Individual CAEVs operate within localized regions and follow realistic trip lengths bounded by the simulated time horizon. The simulated charging infrastructure includes 2 CCNs, 2 SWCNs, 2 DWCNs, 2 LBCNs, 1 AVCN, and 1 GVCN. Charging technologies are assigned such that CCNs, SWCNs, and DWCNs utilize magnetic resonance coupling for WPT, while LBCNs and V2V charging employ LB technology.

UAV placement, as shown in Figure 8, is determined using a simple placement strategy designed to ensure effective coverage, energy efficiency, and operational continuity. EIUAVs are initially deployed from fixed towers that are evenly distributed across the road network, providing uniform spatial coverage for monitoring and dynamic support of CAEV operations. This placement ensures that each vehicle can be reached quickly with minimal travel, while reducing overlapping coverage and energy waste. LBUAVs, which have larger batteries and the ability to wirelessly charge other UAVs, are initially positioned at the center of the operational grid. This centralized placement allows them to efficiently provide on-demand UAV-to-UAV DWC to surrounding EIUAVs, extending mission duration and maximizing operational efficiency. The placement strategy is simple and deterministic, avoiding complex optimization routines while still ensuring robust

coverage and quick access to UAVs requiring support. Once the majority of EIUAVs reach a high SoC, for example above 95%, LBUAVs relocate to a central hub to improve accessibility for maintenance and battery replenishment, minimizing downtime and enhancing system reliability. This initialization approach balances simplicity, coverage, and energy management, providing a practical and effective solution for heterogeneous UAV deployment in dynamic CAEV charging networks.

The simulation was implemented in Python 3.10.10 and executed on a workstation equipped with an NVIDIA RTX A5000 GPU, thus ensuring efficient execution of computationally intensive learning and routing tasks.

To train the SAFE-DDPG agent, we used the parameter settings summarized in Table 6. These values were chosen to complement the architecture and ensure stable, efficient learning under dynamic charging conditions. Moderate actor and critic learning rates provide a balance between convergence speed and training stability, while the small target network update rate (τ) enables gradual policy evolution to prevent instability. The OU noise schedule encourages sufficient exploration in early training and gradually reduces stochasticity as the policy becomes more reliable. Batch size and PER parameters were selected to produce representative, diverse mini-batches while maintaining computational efficiency. Reward weights (β and w terms) and DH-CSP heuristic coefficients (λ values) were tuned to prioritize key operational objectives, such as maximizing charging network utilization, minimizing wait times, and accounting for idle costs, travel overhead, and battery consumption. Network architecture, activation functions, regularization, and dropout choices were selected based on empirical experience and domain knowledge to ensure smooth gradient flow, prevent overfitting, and enhance robustness to variability and noise. These parameters were iteratively refined through preliminary experiments and sensitivity analyses, ensuring that small variations do not compromise learning stability or policy quality. This systematic tuning provides confidence that the agent converges reliably and produces low-variance, high-quality policies. Collectively, these settings enable SAFE-DDPG to learn effective real-time scheduling strategies in heterogeneous charging networks while maintaining computational efficiency and operational reliability.

Training proceeded for approximately 800 episodes, with early stopping applied when the change in cumulative reward between consecutive evaluation intervals fell below a threshold $\Delta = 1.0$, corresponding to a negligible relative improvement given the reward scale (approximately -1480 to -1450). This criterion prevents unnecessary computation once the policy has effectively converged.

The training progression and convergence behavior are discussed in a later section, demonstrating that the agent converges to stable, low-variance policies suitable for real-time scheduling in heterogeneous charging networks.

All simulation results are averaged over 50 independent replications to ensure statistical reliability. Confidence intervals at the 95% level are computed using the Common Random Numbers (CRN) technique combined with the Student's t-distribution, assuming symmetric uncertainty. This approach provides robust estimates of variability and enables meaningful comparisons across different algorithms and scenarios.

The results are presented in three stages. First, we evaluate the charging efficiency of the system using the SoC percentages obtained from a representative simulation run of SAFE-DDPG. This highlights the system's ability to manage energy replenishment effectively. Next, a comparative analysis of the three proposed algorithms including SH-CSP, DH-CSP, and SAFE-DDPG is performed under identical simulation conditions, where average wait time, battery consumption, and travel distances are examined to highlight operational trade-offs. Scalability is subsequently examined by evaluating the trained SAFE-DDPG policy under increasing CAEV load to assess coordination behavior

beyond the baseline configuration. Finally, the vanilla DDPG algorithm is compared with the proposed SAFE-DDPG formulation to isolate the benefits of the safety-, scheduling-, and sustainability-aware enhancements, demonstrating improvements in charging coordination, energy utilization, and wait time reduction. This comparison further supports a mechanism-level ablation analysis to explain the contribution of individual safety, reward, and training stabilization components.

Table 6. Parameter values for SAFE-DDPG.

Parameter	Value	Description
γ	0.99	Discount factor
τ	0.002	Target network update rate
Actor LR	5×10^{-4}	Actor learning rate
Critic LR	1×10^{-3}	Critic learning rate
Batch size	128	Mini-batch size
OU σ_0	0.3	Initial Ornstein–Uhlenbeck (OU) noise amplitude
OU $\sigma_{\min}$	0.05	Minimum OU noise amplitude
OU decay	0.995	OU noise decay rate
PER α	0.5	Prioritization exponent
PER β	$0.4 \rightarrow 1.0$	Annealed importance-sampling weight
PER ϵ	1×10^{-5}	Small constant to avoid zero probabilities
Local reward β_1–β_4	0.3, 0.2, 0.1, 0.1	Weights for immediate reward terms
Global reward $w_{util}, w_{wait}, w_{idle}, w_{travel}, w_{batt}$	1.0, 0.8, 0.3, 0.3, 0.3	Weights for global reward terms
Heuristic λ_1–λ_5	0.10, 0.20, 0.35, 0.20, 0.15	DH-CSP fallback weights
Network Architecture	4 layers (512–256–128–64)	Actor–critic fully connected network
Regularization and Stability	ELU activation, Batch Normalization, L2 5×10^{-5}, Dropout 0.1	Smooth gradients, prevent overfitting, improve training stability
Output and Constraints	Sigmoid activation, reward normalization, gradient clipping	Bounded actions and stable learning

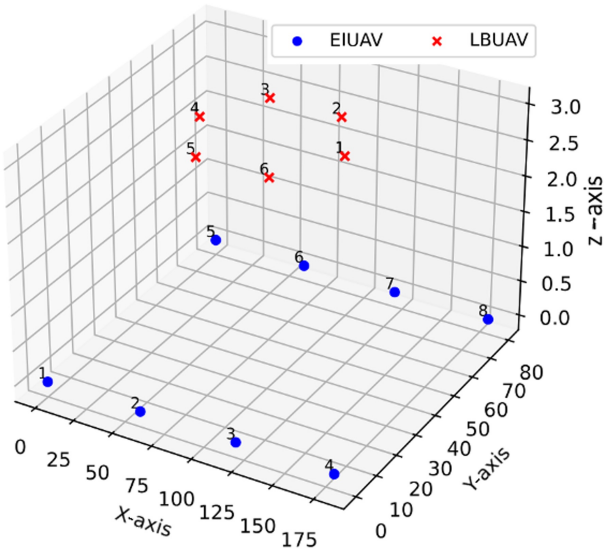


Figure 8. Illustrating the placement of the UAVs.

4.2. System-Level Charging Performance

The charging efficiency of the proposed system is evaluated using aggregated data from a representative simulation run of SAFE-DDPG, covering the entire charging infrastructure in the environment. Figure 9 presents results for the 50 CAEVs, where the first subplot shows the total charging requested through the reservation system (Requested Charge), the amount promised by the system (Reserved Charge), and the amount actually delivered (Delivered Charge). These quantities are aggregated over all charging systems in the simulation and shown as scatter plots to highlight their close correspondence. The second subplot depicts the absolute differences between Requested and Reserved, and between Reserved and Delivered, making visible the minimal gap between these values. With the aid of the proposed misalignment mitigation algorithm, the system achieves an overall charging efficiency of approximately 98.7%**,** meaning nearly all promised energy is successfully delivered. Small discrepancies arise primarily from vehicle misalignment during charging, late arrivals, or unexpected interruptions such as early termination.

A similar analysis is conducted for UAVs, with results shown in Figure 10 for the 6 LBUAVs and 8 EIUAVs. Again, the misalignment mitigation algorithm ensures charging is performed under optimal alignment conditions, leading to a high efficiency of approximately 98.52%**.** The algorithm prioritizes delivering charge such that the majority of user-requested and system-promised energy is fulfilled. The close agreement between requested, reserved, and delivered charge in both CAEV and UAV cases demonstrates the robustness of the charging coordination mechanism across the heterogeneous systems modeled.

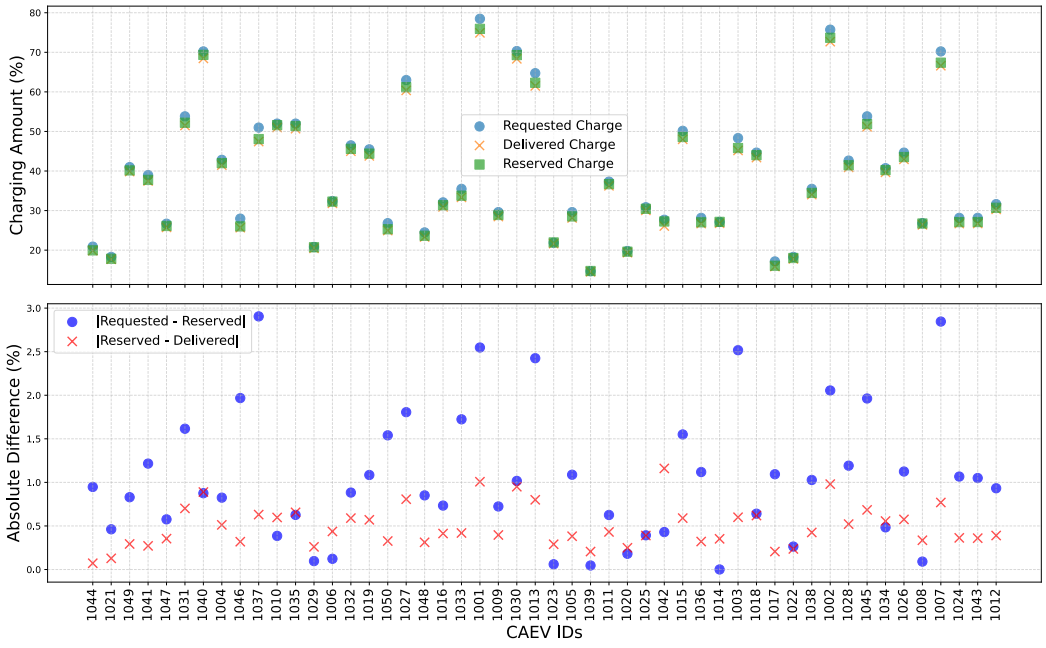


Figure 9. Charging performance for 50 CAEVs under SAFE-DDPG, showing requested, reserved, and delivered charge (in %) and corresponding absolute differences.

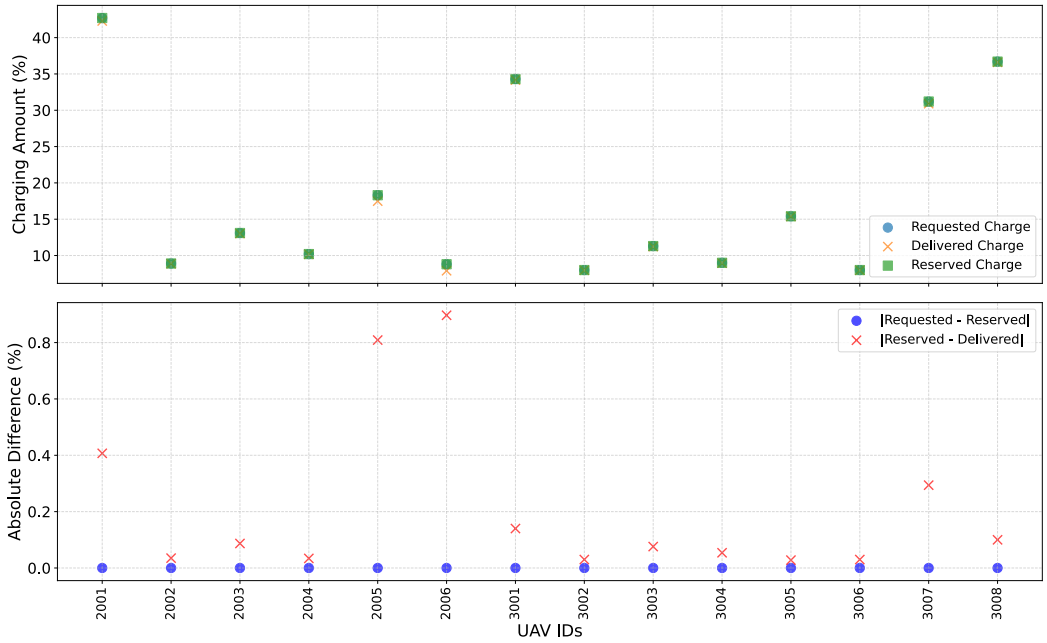


Figure 10. Charging performance for 6 LBUAVs and 8 EIUAVs under SAFE-DDPG, showing requested, reserved, and delivered charge (in %) and corresponding absolute differences.

4.3. Comparison of Proposed Algorithms

The proposed SAFE-DDPG algorithm was evaluated against two proposed baseline strategies: the SH-CSP method, which relies on fixed scheduling without considering dynamic vehicle arrivals, and the DH-CSP method, which accounts for dynamic arrivals but lacks RL capabilities. The comparative results across all performance metrics, as presented in Figures 11 and 12, and Table 7, show that SAFE-DDPG consistently achieves superior outcomes, with DH-CSP providing moderate improvements over SH-CSP.

In terms of average wait time, SAFE-DDPG demonstrates substantial reductions across all CN types. At CCN_1, the average wait time is reduced by 71.2% compared to DH-CSP and by 85.6% compared to SH-CSP. At CCN_2, the improvement reaches 98.4% and 99.2%, respectively, effectively eliminating delays for this node type. SAFE-DDPG also removes waiting entirely at GVCN_1, achieving 0.0 min versus the 0.4667 min of DH-CSP and the 1.1111 min of SH-CSP. Significant gains are also observed in SWCN_2 (50.4% vs. DH-CSP, 65.9% vs. SH-CSP), SWCN_1 (30.0%, 51.1%), LBCN_1 (33.0%, 40.9%), and AVCN_1 (19.7%, 42.8%).

Figure 11 clearly visualizes these trends, with SAFE-DDPG's bars consistently lower across all CN categories. Confidence intervals are constructed using a symmetric Student's t-distribution to quantify uncertainty in the estimated mean wait time across 50 independent simulation replications. While wait time itself is a non-negative quantity, the sampling distribution of the mean is approximately symmetric under moderate sample sizes, even in the presence of skewness or zero-valued observations. In the considered coordinated charging environment, heterogeneous vehicle types, dynamic arrivals, and multiple charging node categories result in some nodes experiencing zero wait time in certain replications and positive delays in others. When aggregated using a symmetric estimator, this variability can produce lower confidence bounds that extend slightly below zero, which is a statistical artifact rather than a physically meaningful negative delay. Importantly, the same confidence interval methodology is applied uniformly across all algorithms, ensuring fair and consistent comparison. Moreover, the tighter and strictly positive intervals observed for SAFE-DDPG reflect its more consistent load balancing and reduced variability across replications.

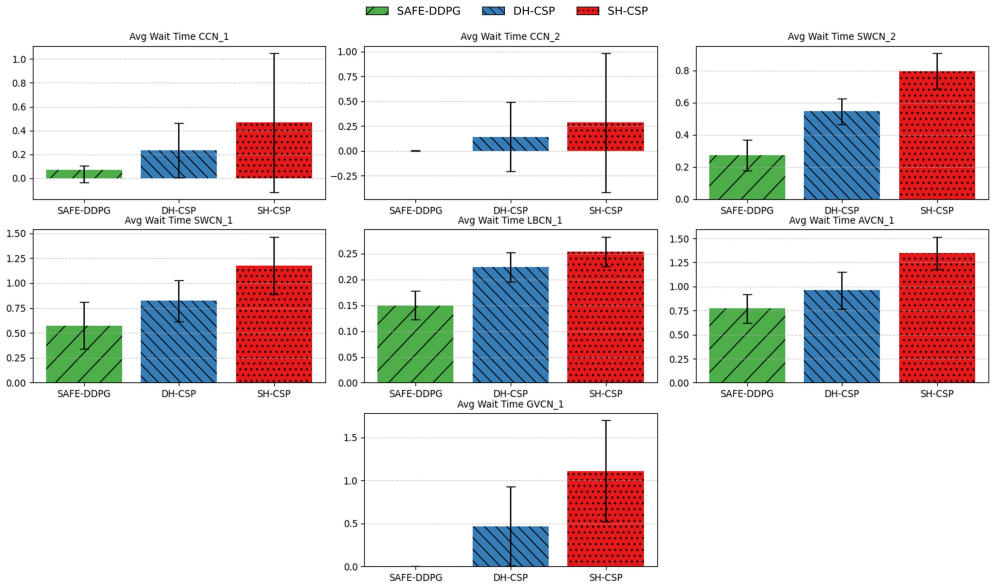


Figure 11. Average wait time per CN type for CAEVs under SAFE-DDPG, DH-CSP, and SH-CSP. Results show consistent reductions across all CN categories for SAFE-DDPG.

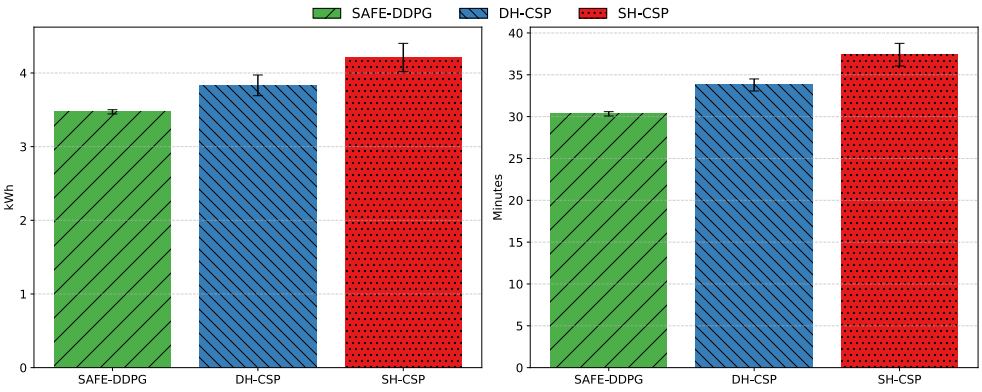


Figure 12. Performance comparison of SAFE-DDPG, DH-CSP, and SH-CSP in terms of (**left**) battery consumption (kWh) and (**right**) travel time (minutes). SAFE-DDPG achieves both lower energy use and shorter trip durations.

Table 7. Quantitative comparison of SAFE-DDPG, DH-CSP, and SH-CSP for all evaluated metrics, including average wait times per CN, battery consumption, and travel time, with percentage improvements of SAFE-DDPG over the baseline methods.

Metric	SAFE-DDPG	DH-CSP	SH-CSP	% vs. DH-CSP	% vs. SH-CSP
Avg. Wait Time CCN_1 (min)	**0.067**	0.234	0.467	**71.20%**	**85.60%**
Avg. Wait Time CCN_2 (min)	**0.00228**	0.1429	0.2857	**98.40%**	**99.20%**
Avg. Wait Time SWCN_2 (min)	**0.2709**	0.5456	0.7954	**50.40%**	**65.90%**
Avg. Wait Time SWCN_1 (min)	**0.5748**	0.8215	1.1754	**30.00%**	**51.10%**
Avg. Wait Time LBCN_1 (min)	**0.1502**	0.2238	0.254	**33.00%**	**40.90%**
Avg. Wait Time AVCN_1 (min)	**0.7706**	0.9599	1.3485	**19.70%**	**42.80%**
Avg. Wait Time GVCN_1 (min)	**0**	0.4667	1.1111	**Eliminates**	**Eliminates (100%)**
Battery Consumption (kWh)	**3.4726**	3.8321	4.2105	**9.30%**	**17.50%**
Travel Cost (min)	**30.33**	33.78	37.41	**10.20%**	**18.90%**

Note: Bold indicates SAFE-DDPG best results and improvements over DH-CSP and SH-CSP.

For SH-CSP, which lacks dynamic arrival handling, some charging nodes remain unused in certain replications, resulting in zero wait times, while other replications record positive waits. DH-CSP, which handles dynamic arrivals, exhibits smaller variability, with lower bounds extending slightly below zero in rare cases due to occasional under-utilization of certain nodes. In contrast, SAFE-DDPG adaptively balances loads across charging nodes, yielding more consistent wait times across replications and consequently tighter, strictly positive confidence intervals.

While the improvements in battery consumption and travel time, shown in Figure 11, are more modest in percentage terms, but they remain operationally significant. SAFE-DDPG reduces battery usage to 3.4726 kWh, which is 9.3% less than DH-CSP and 17.5% less than SH-CSP, therefore directly contributing to greater energy efficiency and longer operational range. Travel time is lowered to 30.33 min, corresponding to reductions of 10.2% and 18.9% compared to DH-CSP and SH-CSP, respectively. Given the inherent constraints of vehicular mobility and charging infrastructure, these gains translate to faster trip completion, reduced congestion, and improved service reliability.

Importantly, the evaluation covers a variety of charging network configurations and vehicle operating contexts. The results confirm that the proposed algorithms are adaptable across diverse network types and vehicle categories. In lower-demand, predictable environments, DH-CSP may be a reasonable choice due to its reduced computational overhead compared to SAFE-DDPG, while still delivering measurable gains over SH-CSP. However, in high-demand, dynamically changing systems, particularly where charging demand is highly variable and route optimization is critical, SAFE-DDPG's RL-driven adaptability makes it the clear recommendation.

From a broader adoption perspective, SAFE-DDPG offers benefits that extend beyond operational efficiency. By reducing wait times to near-zero in several CN categories, improving battery efficiency, and shortening travel times, the system directly addresses key barriers to EV adoption such as range anxiety, charging delays, and uncertainty in trip planning. The charging reservation and trip planning capabilities inherent to the SAFE-DDPG framework ensure drivers can plan journeys with predictable charging stops, thereby increasing confidence in EV usability for both urban commutes and long-distance travel.

Environmentally, the lower energy consumption achieved by SAFE-DDPG reduces the load on the electrical grid and minimizes associated carbon emissions when the electricity mix includes fossil fuels. Over time, widespread adoption of such an efficient scheduling system would enhance the sustainability of EV ecosystems by encouraging more drivers to transition from internal combustion vehicles, knowing that the charging process is predictable, optimized, and minimally disruptive to their travel schedules.

The observed performance advantages of SAFE-DDPG stem from its design elements. These include feasibility awareness, which enforces operational constraints such as vehicle state-of-charge and charging station capacity. Adaptive noise dynamically modulates exploration during learning. Prioritized experience replay focuses updates on the most informative scenarios. The dual-stage reward function balances immediate service objectives with long-term system efficiency. Together, these features enable SAFE-DDPG to outperform heuristic and dynamic baselines across all evaluated metrics.

Although DH-CSP does not match the performance of SAFE-DDPG, it still consistently improves over SH-CSP. For example, DH-CSP reduces average wait times at CCN_1 by 49.9%, at SWCN_2 by 31.4%, and at LBCN_1 by 11.9%, and lowers battery consumption and travel time by approximately 9–10%. These results suggest that dynamic arrival handling is beneficial, but RL–driven optimization substantially amplifies those benefits.

Table 7 summarizes the percentage improvements of SAFE-DDPG over both baselines for all evaluated metrics. The percentage improvements were calculated using the formula:

$$\%\text{Improvement} = \frac{\text{Baseline Value} - \text{SAFE-DDPG Value}}{\text{Baseline Value}} \times 100 \quad (58)$$

The combined evidence from Figures 10 and 11, and Table 7 underscores the consistent and statistically significant advantages of SAFE-DDPG in reducing delays, conserving energy, and improving travel efficiency across all charging network types. Its ability to support environmental sustainability and encourage broader electric vehicle adoption makes it the most effective and future-proof solution among the evaluated approaches.

4.4. Scalability Under Varying Load

The proposed framework is designed to support large-scale deployments from both an architectural and an algorithmic perspective. Architecturally, the hybrid coordination topology with CNMs enables incremental integration of additional charging nodes and vehicles without modifying the scheduling logic, as coordination is handled locally and decisions are generated on a per-request basis. Algorithmically, scalability is assessed by evaluating the same trained SAFE-DDPG policy under increasing CAEV load using Jain's Fairness Index (JFI) [79]. As shown in Table 8, fairness remains high as demand increases, with degradation occurring gradually only as infrastructure approaches saturation. This indicates that coordination performance scales with system load and that practical limits are governed primarily by available charging capacity rather than algorithmic constraints.

Table 8. Overall fairness under increasing CAEV load using SAFE-DDPG.

CAEV Load	Overall JFI	Observed Trend
50	0.857	Low contention regime
100	0.921	Increasing coordination balance
200	0.927	Peak balanced utilization
400	0.867	High load saturation regime

4.5. SAFE-DDPG vs. Vanilla DDPG

The comparison between vanilla DDPG and SAFE-DDPG highlights how SAFE-DDPG's targeted design modifications result in a more robust, fair, and efficient policy for large-scale online CAEV scheduling. Vanilla DDPG was trained with the same neural architecture, 24-dimensional state–action representation, and immediate reward signals for a fair comparison. Unlike vanilla DDPG, SAFE-DDPG employs a dual-stage reward structure, combining local, immediate rewards with global network-wide feedback, along with adaptive noise modulation and feasibility-aware action screening. These mechanisms enable broad exploration in early training, refined exploitation later, and balanced resource allocation across all CNs. From the training curves (Figures 13 and 14), SAFE-DDPG achieves more reliable convergence and higher-quality policies, while vanilla DDPG often converges myopically to a lower-quality local optimum, overusing a subset of CNs and leaving others largely idle.

Server utilization (Figure 15) and throughput performance (Figure 16) highlight the difference in resource allocation. Vanilla DDPG tends to concentrate assignments on a few CNs, leaving many others idle. As a result, metrics for these underutilized CNs can be missing or zero, which may give a misleading impression of performance if interpreted individually. In contrast, SAFE-DDPG distributes vehicles more evenly across all CNs, ensuring better coverage and more effective use of available resources. This demonstrates that evaluating system-wide performance, rather than individual CN metrics, is crucial for a fair and realistic comparison between policies. Feasibility-aware action filtering is primarily active during early training. As the policy converges, fallback usage decreases

from approximately 0.2 of decisions to near zero, indicating that feasibility constraints are learned rather than inherited from the DH-CSP heuristic.

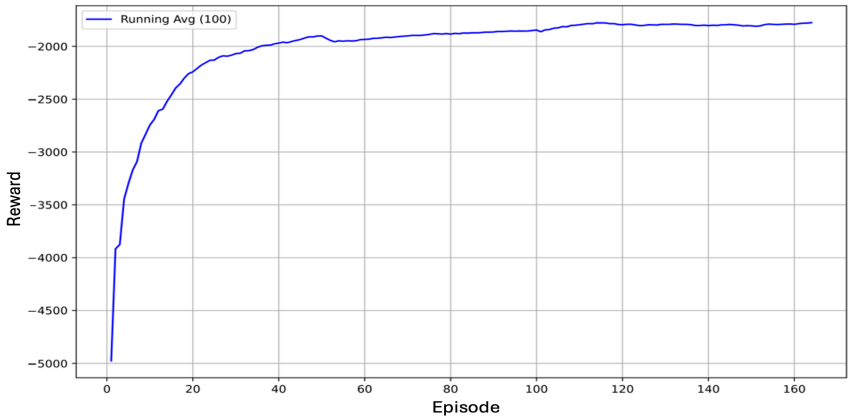


Figure 13. Training reward progression for vanilla DDPG.

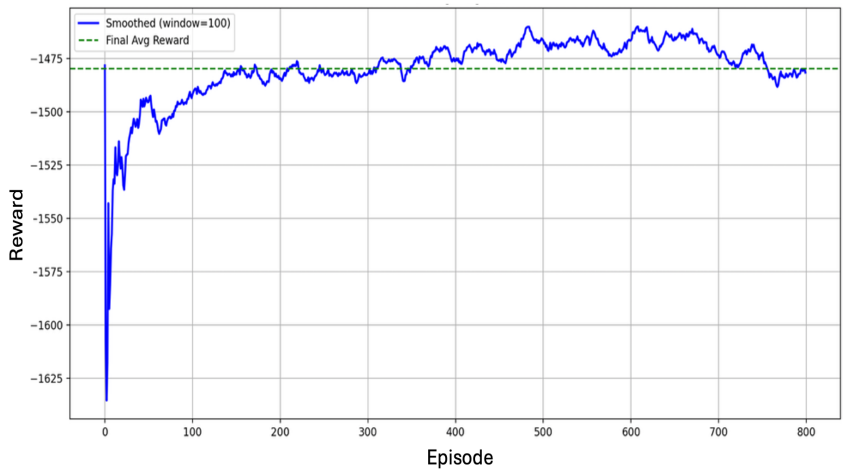


Figure 14. Training reward progression for SAFE-DDPG.

In terms of average wait times (Figure 17), SAFE-DDPG consistently reduces delays compared to vanilla DDPG. The local reward discourages load imbalance and excessive travel, while the global reward penalizes idle capacity and waiting time, promoting pre-emptive vehicle distribution to avoid congestion. PER further enhances learning by emphasizing high-impact scenarios such as peak demand, congestion avoidance, and long-distance routing. As a result, average battery consumption decreases from 4.57 kWh to 3.47 kWh (24.02% reduction) and travel time from approximately 40 min to 30 min (24.09% reduction) (Figure 18).

Collectively, SAFE-DDPG's combination of adaptive noise modulation, dual-stage reward design, feasibility-aware action screening, and prioritized experience replay produces a policy that outperforms vanilla DDPG in fairness, stability, and operational efficiency. Its topology-agnostic state–action representation and balanced reward incentives allow learned policies to generalize across different network layouts and traffic conditions without retraining. These results demonstrate that SAFE-DDPG is operationally efficient, robust, and scalable, providing a practical and reliable solution for dynamic, heterogeneous CAEV scheduling in real-world smart transportation networks.

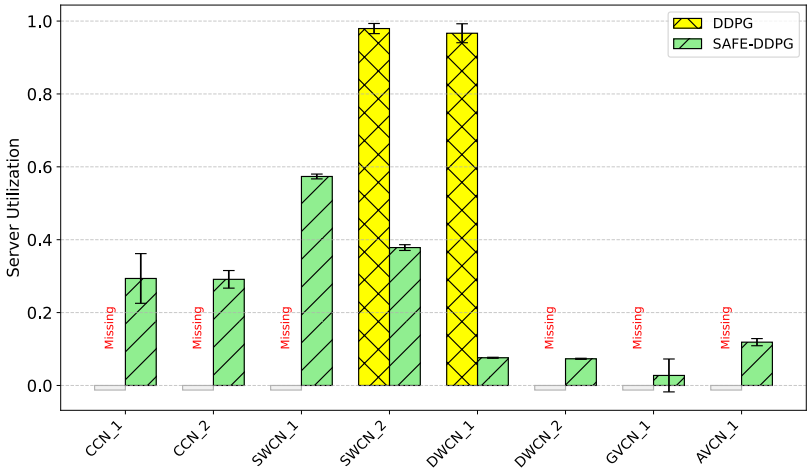


Figure 15. Server utilization comparison between vanilla DDPG and SAFE-DDPG, illustrating SAFE-DDPG's balanced usage (0.03–0.57) across all servers enabled by feasibility-aware action screening, reducing idle capacity and overloading.

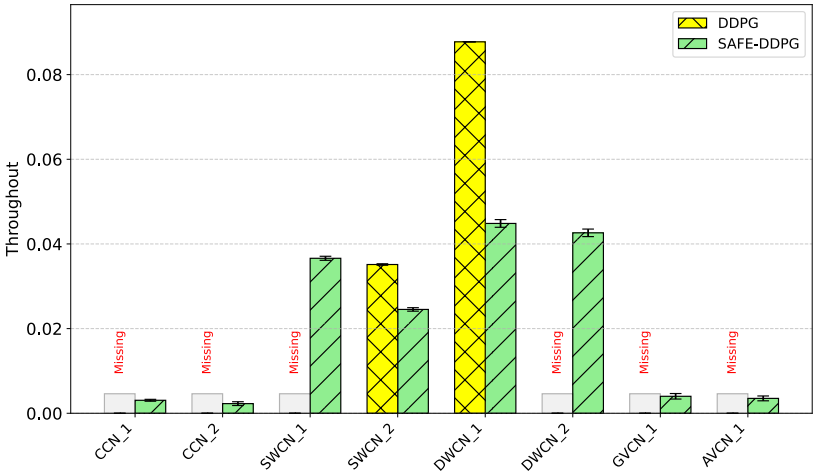


Figure 16. Throughput comparison between vanilla DDPG and SAFE-DDPG across different charging network nodes. SAFE-DDPG achieves higher and more balanced throughput across all servers, while vanilla DDPG leaves many servers idle, resulting in missing throughput values for several nodes.

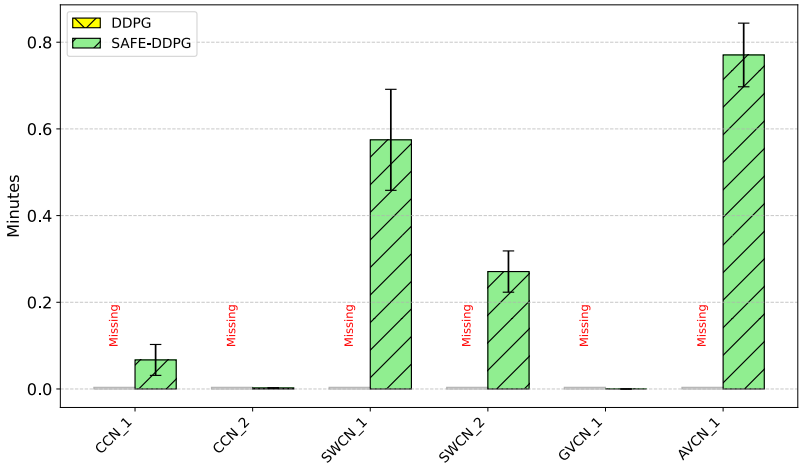


Figure 17. Average wait time per server under vanilla DDPG and SAFE-DDPG, demonstrating SAFE-DDPG's consistent delay reduction through its dual-stage reward structure that discourages load imbalance and excessive travel.

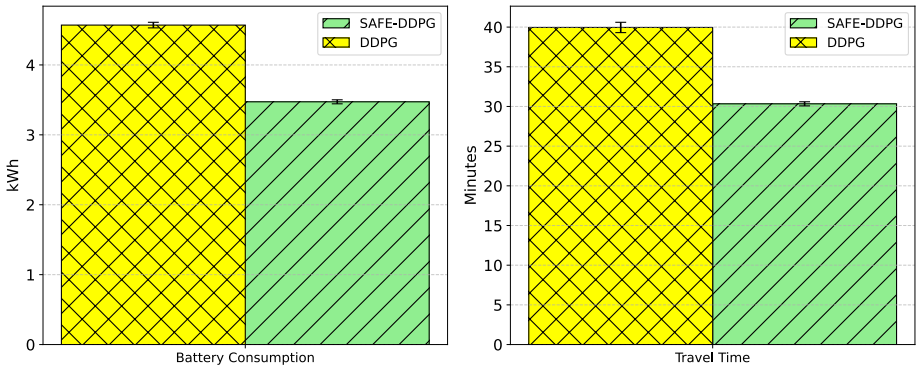


Figure 18. Comparison of battery consumption (**left**) and travel time (**right**) for vanilla DDPG and SAFE-DDPG.

4.6. Ablation and Mechanism Contribution Analysis

The contribution of individual mechanisms in SAFE-DDPG is assessed through comparison with an unconstrained learning-based scheduler that omits feasibility, safety, and stabilization features, since disabling these components individually would lead to infeasible or unsafe charging behavior. As summarized in Table 9, feasibility-aware action filtering and safety-constrained decision enforcement provide the largest benefits among all added components by preventing invalid actions and substantially improving coordination quality. Reward shaping further reduces congestion and waiting delays, while guided fallback and load-aware state representation stabilize training and support generalization under higher demand. Together, these mechanisms explain the robustness and consistency of SAFE-DDPG under dynamic operating conditions.

Table 9. Observed contribution of SAFE-DDPG mechanisms.

Mechanism	Observed Impact
Feasibility and safety constraints	20–30% lower charging fulfillment and fairness reduction from ∼0.85 to ∼0.62 when unconstrained
Reward shaping	50–80% higher wait time at congested nodes under imbalanced coordination
Guided fallback and exploration	Higher variance and unstable behavior during early training
State representation	Increased congestion sensitivity as demand exceeds training levels

5. Conclusions and Future Work

This paper has introduced a three-layer architecture combining a handshake protocol, a wireless charging misalignment correction algorithm, and three scheduling strategies: SH-CSP, DH-CSP, and SAFE-DDPG to address key gaps in coordinated CAEV–UAV charging. The framework jointly tackles dynamic arrivals, cross-network fairness, and operational feasibility across heterogeneous CN types, including static, dynamic, and V2V configurations, employing magnetic resonance and laser beaming charging technologies. SAFE-DDPG extends vanilla DDPG into a domain-optimized, feasibility-aware, safety-critical, and computationally efficient controller, integrating a dual-stage reward structure, feasibility-aware action screening, and stability-oriented neural design.

Across simulations, SAFE-DDPG reduced average wait times by more than 70% compared to DH-CSP and over 85% compared to SH-CSP in high-demand nodes, cut average battery consumption by 9–18%, and shortened travel times by 10–19% over heuristic baselines. With the proposed misalignment mitigation algorithm, charging efficiency consistently remained around 98% for both CAEVs and UAVs across all CN types. Against

vanilla DDPG, SAFE-DDPG achieved more reliable convergence, a 24% reduction in both average battery consumption and travel time, more balanced utilization across heterogeneous charging networks, and higher throughput fairness, and stable coordination behavior under increasing load. These gains stem from its adaptive exploration, PER, feasibility checks, and reward design balancing short-term performance with long-term sustainability whose individual contributions were examined through mechanism-level ablation analysis.

Future work will extend SAFE-DDPG to multi-agent fleet coordination, incorporate renewable energy and V2G interactions, and develop domain-adaptive RL methods for transferring policies across cities with varying infrastructure and traffic patterns while maintaining efficiency and robustness.

Author Contributions: Conceptualization, P.W.S. and H.T.M.; methodology, P.W.S., H.T.M. and B.K.; software, P.W.S.; validation, H.T.M. and B.K.; formal analysis, P.W.S.; investigation, P.W.S.; visualization, P.W.S.; writing—original draft preparation, P.W.S.; writing—review and editing, P.W.S. and B.K.; supervision, H.T.M. and B.K.; project administration, H.T.M. and B.K.; funding acquisition, H.T.M. and B.K. All authors have read and agreed to the published version of the manuscript.

Funding: This work was supported in part by the Natural Sciences and Engineering Research Council of Canada (NSERC) Research Grant numbers RGPIN-2023-03393, RGPIN-2024-06110 and the NSERC CREATE TRAVERSAL Program, and in part by Ontario Research Fund-Research Excellence (ORF-RE) under grant number RE12-024.

Data Availability Statement: Data are available upon request.

Conflicts of Interest: The authors declare no conflicts of interest.

Abbreviations

The following abbreviations are used in this manuscript:

3GPP	3rd Generation Partnership Project
A2C	Advantage Actor-Critic
AI	Artificial Intelligence
AoI	Age-of-Information
AVCN	Aerial Vehicle Charging Network
AVCNM	Aerial Vehicle Charging Network Manager
CAEV	Connected and Autonomous Electric Vehicle
CCN	Cabled Charging Network
CCNM	Cabled Charging Network Manager
CN	Charging Network
CNM	Charging Network Manager
CP	Credit Point
CPT	Capacitive Power Transfer
CRN	Common Random Numbers
CRV	Charge Receiving Vehicle
CDV	Charge Delivery Vehicle
DH-CSP	Dynamic Heuristic Charging Scheduling and Planning
DQN	Deep Q-Network
DDPG	Deep Deterministic Policy Gradient
DRL	Deep Reinforcement Learning
DWC	Dynamic Wireless Charging
DWCN	Dynamic Wireless Charging Network
DWCNM	Dynamic Wireless Charging Network Manager
EDC	Energy Distribution Center
EIUAV	Edge Intelligent Uncrewed Aerial Vehicle

ESP	Energy Service Provider
EVCRP	Electric Vehicle Charging Routing Problem
EVSE	Electric Vehicle Supply Equipment
FC-TDTA	Fair Charging–Trajectory Design Time Allocation
GVCN	Ground Vehicle Charging Network
GVCNM	Ground Vehicle Charging Network Manager
IEC	Intelligent Edge Computing
IPT	Inductive Power Transfer
IoT	Internet of Things
ISAC	Integrated Sensing and Communication
ITU	International Telecommunication Union
ITS	Intelligent Transportation System
JFI	Jain's Fairness Index
KDC	Key Distribution Center
LB	Laser Beaming
LBCN	Laser-Beaming Charging Network
LBCNM	Laser-Beaming Charging Network Manager
LBUAV	Laser-Beaming Uncrewed Aerial Vehicle
LB-WPT	Laser Beaming Wireless Power Transfer
Li-Fi	Light Fidelity
LOS	Line-of-Sight
LSTM	Long Short-Term Memory
MR	Magnetic Resonance
MR-WPT	Magnetic Resonance Wireless Power Transfer
mMTC	Massive Machine-Type Communications
NGMN	Next Generation Mobile Networks
NOMA	Non-Orthogonal Multiple Access
OOK	On–Off Keying
OU	Ornstein–Uhlenbeck
OWPT	Optical Wireless Power Transfer
PER	Prioritized Experience Replay
P2P	Peer-to-Peer
POMDP	Partially Observable Markov Decision Process
PPO	Proximal Policy Optimization
QoS	Quality of Service
RFID	Radio-Frequency Identification
RL	Reinforcement Learning
RSU	Roadside Unit
SAE	Society of Automotive Engineers
SAC	Soft Actor-Critic
SAFE-DDPG	Safety, Scheduling, and Sustainability-Aware Feasibility-Enhanced Deep Deterministic Policy Gradient
SH-CSP	Static Heuristic Charging Scheduling and Planning
SUMO	Simulation of Urban MObility
SWC	Static Wireless Charging
SWCN	Static Wireless Charging Network
SWCNM	Static Wireless Charging Network Manager
TD	Temporal Difference
TD3	Twin Delayed Deep Deterministic Policy Gradient
UAV	Uncrewed Aerial Vehicle
URLLC	Ultra-Reliable Low-Latency Communication
V2G	Vehicle-to-Grid
V2I	Vehicle-to-Infrastructure
V2V	Vehicle-to-Vehicle

WPT	Wireless Power Transfer
SoC	State of Charge

Appendix A. UAV Mobility and Propulsion Power Model

This appendix presents the detailed rotary-wing UAV propulsion power model used to capture mobility-dependent energy consumption in the proposed framework. The intermediate expressions for hovering, horizontal flight, and vertical motion are provided to preserve physical rigor and reproducibility. The resulting compact mobility-aware propulsion power expression used in scheduling and learning is given in Equation (1) in the main text.

Appendix A.1. Hover Power Consumption

The first component of the UAV propulsion model is the total hovering power, P_{mhov}, which accounts for blade profile and induced power losses. It depends on the UAV weight W, number of rotors n, rotor radius r, rotor disk area $A = \pi r^2$, thrust coefficient C_T, air density ρ, profile drag coefficient δ_s, and induced power correction factor k. The hovering power is expressed as follows:

$$P_{mhov} = \frac{\delta_s}{8}\sqrt{\frac{n}{\rho A}}\left(\frac{W}{C_T}\right)^{3/2} + (1+k)\frac{W^{3/2}}{\sqrt{2n\rho A}} \tag{A1}$$

Appendix A.2. Horizontal Flight Power Component

When the UAV moves horizontally at a constant velocity V_h, the propulsion power increases due to parasitic drag and changes in induced velocity. In addition to the parameters above, this regime introduces the induced velocity in hover v_0 and the equivalent flat plate area for horizontal drag $SFP_{\parallel}$. The horizontal flight power is modeled as follows:

$$\begin{aligned} P_{mf}(V_h) = {} & \frac{\delta_s}{8}\sqrt{\frac{n}{\rho A}}\left(\frac{W}{C_T}\right)^{3/2} + \frac{3\delta_s}{8}\sqrt{\frac{Wn\rho A}{C_T}}\,V_h^2 \\ & + (1+k)\frac{W^{3/2}}{\sqrt{2n\rho A}}\left(\sqrt{1+\frac{V_h^4}{4v_0^4}} - \frac{V_h^2}{2v_0^2}\right) + \frac{n}{2}SFP_{\parallel}\rho V_h^3 \end{aligned} \tag{A2}$$

Appendix A.3. Vertical Ascent and Descent Power Component

Vertical motion, either ascent or descent, is modeled using the vertical velocity V_v and the sign function $\mathrm{sgn}(V_v)$, which returns $+1$ for ascent and -1 for descent. This formulation also uses $SFP_{\perp}$, the equivalent flat plate area for vertical drag. A unified expression for both ascent and descent is given by the following:

$$\begin{aligned} P_{mv}(V_v) = {} & P_{mhov} + \frac{1}{2}W|V_v| + \mathrm{sgn}(V_v)\,\frac{n}{4}SFP_{\perp}\rho|V_v|^3 \\ & + \left(\frac{W}{2} + \mathrm{sgn}(V_v)\,\frac{n}{4}SFP_{\perp}\rho V_v^2\right)\sqrt{\left(1+\mathrm{sgn}(V_v)\,\frac{SFP_{\perp}}{A}\right)V_v^2 + \frac{2W}{n\rho A}} \end{aligned} \tag{A3}$$

Appendix A.4. Energy Consumption and Relevance to Mobility-Aware Scheduling

The propulsion power components derived above are combined in the main text into the compact total propulsion power expression given in Equation (1), which captures hovering, horizontal cruising, vertical ascent and descent, and combined three-dimensional maneuvers. This formulation enables computationally efficient estimation of UAV energy consumption while preserving physical interpretability.

The resulting mobility-aware power model directly affects residual energy estimation, arrival timing, alignment duration, and charging feasibility, and is therefore used by both heuristic and learning-based schedulers under realistic UAV motion dynamics.

References

1. Shaikh, P.W.; Mouftah, H.T. Intelligent Charging Infrastructure Design for Connected and Autonomous Electric Vehicles in Smart Cities. In Proceedings of the IM 2021—2021 IFIP/IEEE International Symposium on Integrated Network Management, Virtual, 17–21 May 2021; pp. 992–997.
2. Shaikh, P.W.; Mouftah, H.T. Connected and Autonomous Electric Vehicles Charging Reservation and Trip Planning System. In Proceedings of the 2021 International Wireless Communications and Mobile Computing, IWCMC 2021, Harbin, China, 28 June–2 July 2021; pp. 1135–1140. [CrossRef]
3. Vaidya, B.; Mouftah, H.T. Deploying Wireless Charging Systems for Connected and Autonomous Electric Vehicles. In *Connected and Autonomous Vehicles in Smart Cities*; CRC Press: Boca Raton, FL, USA, 2020; pp. 387–405. [CrossRef]
4. Sadeghi, M.; Erol-Kantarci, M.; Mouftah, H.T. Connected and Autonomous Electric Vehicle Charging Infrastructure Integration to Microgrids in Future Smart Cities. In *Connected and Autonomous Vehicles in Smart Cities*; CRC Press: Boca Raton, FL, USA, 2020; pp. 1–17. [CrossRef]
5. Segala, G.; Bassoli, R.; Granelli, F.; Fitzek, F.H.P. Connected Unmanned Aerial Vehicles for Flexible Coverage, Data Gathering and Emergency Scenarios. In *Connected and Autonomous Vehicles in Smart Cities*; CRC Press: Boca Raton, FL, USA, 2020; pp. 277–291. [CrossRef]
6. Hanafiah, M.H.M.; Al-Humairi, S.N.S.; Taib, M.A.A.M.; Jaharadak, A.A. Analysis and Optimization of Care-purpose Drone For Medical-Based Applications. In Proceedings of the 2024 20th IEEE International Colloquium on Signal Processing and Its Applications, CSPA 2024—Conference Proceedings, Langkawi, Malaysia, 1–2 March 2024; pp. 184–189. [CrossRef]
7. Zhu, Q.; Zheng, J. Coverage Performance Analysis of Backhaul-Limited UAV-Assisted Cellular Networks. *IEEE Int. Conf. Commun.* **2023**, *2023*, 6523–6528. [CrossRef]
8. Sharma, A.; Singh, P.K. Applicability of UAVs in detecting and monitoring burning residue of paddy crops with IoT Integration: A step towards greener environment. *Comput. Ind. Eng.* **2023**, *184*, 109524. [CrossRef]
9. Souilem, M.; Dghais, W.; Radwan, A. Wirelessly Powered Unmanned Aerial Vehicles (UAVs) in Smart City. In *Connected and Autonomous Vehicles in Smart Cities*; CRC Press: Boca Raton, FL, USA, 2020; pp. 437–456. [CrossRef]
10. Alwis, C.D.; Kalla, A.; Pham, Q.V.; Kumar, P.; Dev, K.; Hwang, W.J.; Liyanage, M. Survey on 6G Frontiers: Trends, Applications, Requirements, Technologies and Future Research. *IEEE Open J. Commun. Soc.* **2021**, *2*, 836–886. [CrossRef]
11. Lv, Z.; Qiao, L.; You, I. 6G-Enabled Network in Box for Internet of Connected Vehicles. *IEEE Trans. Intell. Transp. Syst.* **2021**, *22*, 5275–5282. [CrossRef]
12. Bisio, I.; Garibotto, C.; Haleem, H.; Lavagetto, F.; Sciarrone, A. A Systematic Review of Drone Based Road Traffic Monitoring System. *IEEE Access* **2022**, *10*, 101537–101555. [CrossRef]
13. Chittoor, P.K.; Chokkalingam, B.; Mihet-Popa, L. A Review on UAV Wireless Charging: Fundamentals, Applications, Charging Techniques and Standards. *IEEE Access* **2021**, *9*, 69235–69266. [CrossRef]
14. Environment and Climate Change Canada (ECCC). *Where Canada's Greenhouse Gas Emissions Come from: 2024 National Greenhouse Gas Inventory*; Government of Canada: Ottawa, ON, Canada, 2025.
15. Abbas, M.T.; Grinnemo, K.-J.; Ferré, G.; Laurent, P.; Alfredsson, S.; Rajiullah, M.; Eklund, J. Towards zero-energy: Navigating the future with 6G in Cellular Internet of Things. *J. Netw. Comput. Appl.* **2024**, *230*, 103945. [CrossRef]
16. Government of Canada. *Net-Zero Emissions by 2050*; Government of Canada: Ottawa, ON, Canada, 2025.
17. Bushnaq, O.M.; Mishra, D.; Natalizio, E.; Akyildiz, I.F. Unmanned aerial vehicles (UAVs) for disaster management. In *Nanotechnology-Based Smart Remote Sensing Networks for Disaster Prevention*; Elsevier: Amsterdam, The Netherlands, 2022; pp. 159–188. [CrossRef]
18. Ojdanic, D.; Sinn, A.; Naverschnigg, C.; Schitter, G. Feasibility Analysis of Optical UAV Detection Over Long Distances Using Robotic Telescopes. *IEEE Trans. Aerosp. Electron. Syst.* **2023**, *59*, 5148–5157. [CrossRef]
19. Alotaibi, J.; Oubbati, O.S.; Atiquzzaman, M.; Alromithy, F.; Altimania, M.R. Optimizing disaster response with UAV-mounted RIS and HAP-enabled edge computing in 6G networks. *J. Netw. Comput. Appl.* **2025**, *241*, 104213. [CrossRef]
20. Mahbub, M.; Saym, M.M.; Jahan, S.; Paul, A.K.; Vahid, A.; Hosseinalipour, S.; Barua, B.; Yeh, H.-G.; Shubair, R.M.; Taleb, T. A holistic survey of UAV-assisted wireless communications in the transition from 5G to 6G: State-of-the-art intertwined innovations, challenges, and opportunities. *J. Netw. Comput. Appl.* **2025**, *237*, 104131. [CrossRef]
21. Lin, C.H.; Amir, M.; Tariq, M.; Shahvez, M.; Alamri, B.; Alahmadi, A.; Siddiqui, M.; Beig, A.R. Comprehensive Analysis of IPT v/s CPT for Wireless EV Charging and Effect of Capacitor Plate Shape and Foreign Particle on CPT. *Processes* **2021**, *9*, 1619. [CrossRef]
22. Nguyen, D.H. Dynamic Optical Wireless Power Transfer for Electric Vehicles. *IEEE Access* **2023**, *11*, 2787–2795. [CrossRef]

23. Goyal, R.; Tomar, A. Dynamic Charging Scheduling and Path Planning Scheme for Multiple MC-enabled On-demand Wireless Rechargeable Sensor Networks. *J. Netw. Comput. Appl.* **2024**, *230*, 103943. [CrossRef]
24. Kirubasri, G.; Sankar, S.; Pandey, D.; Pandey, B.K.; Singh, H.; Anand, R. A Recent Survey on 6G Vehicular Technology, Applications and Challenges. In Proceedings of the 2021 9th International Conference on Reliability, Infocom Technologies and Optimization (Trends and Future Directions), ICRITO 2021, Noida, India, 3–4 September 2021. [CrossRef]
25. Akbar, M.S.; Hussain, Z.; Ikram, M.; Sheng, Q.Z.; Mukhopadhyay, S.C. On challenges of sixth-generation (6G) wireless networks: A comprehensive survey of requirements, applications, and security issues. *J. Netw. Comput. Appl.* **2025**, *233*, 104040. [CrossRef]
26. Duong, T.Q.; Kim, K.J.; Kaleem, Z.; Bui, M.P.; Vo, N.S. UAV caching in 6G networks: A Survey on models, techniques, and applications. *Phys. Commun.* **2022**, *51*, 101532. [CrossRef]
27. Xu, D.; Li, T.; Li, Y.; Su, X.; Tarkoma, S.; Jiang, T.; Crowcroft, J.; Hui, P. Edge Intelligence: Empowering Intelligence to the Edge of Network. *Proc. IEEE* **2021**, *109*, 1778–1837. [CrossRef]
28. Qi, W.; Li, Q.; Song, Q.; Guo, L.; Jamalipour, A. Extensive Edge Intelligence for Future Vehicular Networks in 6G. *IEEE Wirel. Commun.* **2021**, *28*, 128–135. [CrossRef]
29. Faraci, G.; Rizzo, S.A.; Schembra, G. Green Edge Intelligence for Smart Management of a FANET in Disaster-Recovery Scenarios. *IEEE Trans. Veh. Technol.* **2023**, *72*, 3819–3831. [CrossRef]
30. Hortelano, D.; de Miguel, I.; Barroso, R.J.D.; Aguado, J.C.; Merayo, N.; Ruiz, L.; Asensio, A.; Masip-Bruin, X.; Fernández, P.; Lorenzo, R.M.; et al. A comprehensive survey on reinforcement-learning-based computation offloading techniques in Edge Computing Systems. *J. Netw. Comput. Appl.* **2023**, *216*, 103669. [CrossRef]
31. Wang, L.; Zhou, W.; Zhai, L. Task offloading strategy of vehicle edge computing based on reinforcement learning. *J. Netw. Comput. Appl.* **2025**, *239*, 104195. [CrossRef]
32. Wong, A.; Bäck, T.; Kononova, A.V.; Plaat, A. Deep multiagent reinforcement learning: Challenges and directions. *Artif. Intell. Rev.* **2023**, *56*, 5023–5056. [CrossRef]
33. Matsuo, Y.; LeCun, Y.; Sahani, M.; Precup, D.; Silver, D.; Sugiyama, M.; Uchibe, E.; Morimoto, J. Deep learning, reinforcement learning, and world models. *Neural Netw.* **2022**, *152*, 267–275. [CrossRef] [PubMed]
34. DeepMind. *Deep Reinforcement Learning*; DeepMind: London, UK, 2016.
35. Jin, J.; Xu, Y. Shortest-Path-Based Deep Reinforcement Learning for EV Charging Routing Under Stochastic Traffic Condition and Electricity Prices. *IEEE Internet Things J.* **2022**, *9*, 22571–22581. [CrossRef]
36. Zhang, Y.; Li, M.; Chen, Y.; Chiang, Y.Y.; Hua, Y. A Constraint-Based Routing and Charging Methodology for Battery Electric Vehicles With Deep Reinforcement Learning. *IEEE Trans. Smart Grid* **2023**, *14*, 2446–2459. [CrossRef]
37. Erust, A.C.; Beyazit, M.A.; Tascikaraoglu, F.Y.; Tascikaraoglu, A. Deep Reinforcement Learning-Based Navigation Strategy for a Mobile Charging Station in a Dynamic Environment. In Proceedings of the 2023 International Conference on Smart Energy Systems and Technologies, SEST 2023, Mugla, Turkiye, 4–6 September 2023. [CrossRef]
38. Zhang, J.; Kong, L.; Zhang, H. Coordinated Ride-hailing Order Scheduling and Charging for Autonomous Electric Vehicles Based on Deep Reinforcement Learning. In Proceedings of the 2023 IEEE IAS Industrial and Commercial Power System Asia, I and CPS Asia 2023, Chongqing, China, 7–9 July 2023; pp. 2038–2044. [CrossRef]
39. Li, X.; Ming, F.; Hu, J.; Xu, Z.; Liu, K.; Gao, F.; Guan, X. A Constrained Deep Reinforcement Learning Approach for Charging Scheduling of a Battery Swapping Station. *IEEE Trans. Intell. Transp. Syst.* **2025**, *26*, 20549–20561. [CrossRef]
40. Rahali, H.; Poddubnyy, A.; Nguyen, P. A Comparison of Model-Based and Model-Free Offline Reinforcement Learning Methods for Electric Vehicle Smart Charging Optimization. In Proceedings of the 2025 IEEE Power & Energy Society General Meeting (PESGM), Austin, TX, USA, 27–31 July 2025; pp. 1–5. [CrossRef]
41. Mousaei, A.; Naderi, Y.; Arif, S.M.; Bayram, I.S. Voltage Stability Enhancement in IEEE 14-Bus System Using Deep Deterministic Policy Gradient for EV Charging Management. In Proceedings of the 2025 10th IEEE Workshop on the Electronic Grid (eGRID), Glasgow, UK, 30 September–2 October 2025; pp. 1–6. [CrossRef]
42. Zhu, B.; Bedeer, E.; Nguyen, H.H.; Barton, R.; Gao, Z. UAV Trajectory Planning for AoI-Minimal Data Collection in UAV-Aided IoT Networks by Transformer. *IEEE Trans. Wirel. Commun.* **2023**, *22*, 1343–1358. [CrossRef]
43. Liu, X.; Liu, H.; Zheng, K.; Liu, J.; Taleb, T.; Shiratori, N. AoI-Minimal Clustering, Transmission and Trajectory Co-Design for UAV-Assisted WPCNs. *IEEE Trans. Veh. Technol.* **2025**, *74*, 1035–1051. [CrossRef]
44. Zhang, Z.; Wang, J.; Chen, J.; Zhang, Y.; Sun, Y.; Jiang, C. AoI-Minimal Data Collection in Multi-UAV Assisted Pre-Clustered IoT Networks. In Proceedings of the GLOBECOM 2024—2024 IEEE Global Communications Conference, Cape Town, South Africa, 8–12 December 2024; pp. 2003–2008. [CrossRef]
45. Liu, C.; Guo, Y.; Li, N.; Song, X. AoI-Minimal Task Assignment and Trajectory Optimization in Multi-UAV-Assisted IoT Networks. *IEEE Internet Things J.* **2022**, *9*, 21777–21791. [CrossRef]
46. Huang, S.C.; Yen, L.H.; Chen, Y.W. DRL-Based UAV Serving and Charging Scheduling for Autonomous Service Provisioning. In Proceedings of the 2025 International Conference on Information Networking (ICOIN), Chiang Mai, Thailand, 15–17 January 2025; pp. 323–328. [CrossRef]

47. Ma, H.; Liu, W.; Yang, G.; Sun, H.; Qu, D.; Yang, H. Efficient Charging Coverage Strategy of UAV Based on Improved Deep Reinforcement Learning. *IEEE Trans. Veh. Technol.* **2025**, *74*, 11832–11844. [CrossRef]
48. Chen, H.; He, J.; Li, Y.; Zhao, M.; Tang, F.; Kato, N. Optimizing Smart Wireless Charging and Data Acquisition for UAVs with Battery Life Prediction. *IEEE Trans. Veh. Technol.* **2025**, 1–13. [CrossRef]
49. Panahi, F.H.; Panahi, F.H. Cellular Coverage Extension Using an Intelligent FSO-Based UAV: An Energy and Spectral Efficient Approach. *IEEE Trans. Cogn. Commun. Netw.* **2024**, *11*, 556–565. [CrossRef]
50. Zhang, Z.; Xu, C.; Li, Z.; Zhao, X.; Wu, R. Deep Reinforcement Learning for Aerial Data Collection in Hybrid Powered NOMA-IoT Networks. *IEEE Internet Things J.* **2022**, *10*, 1761–1774. [CrossRef]
51. Xiong, Z.; Zhang, Y.; Lim, W.Y.B.; Kang, J.; Niyato, D.; Leung, C.; Miao, C. UAV-Assisted Wireless Energy and Data Transfer with Deep Reinforcement Learning. *IEEE Trans. Cogn. Commun. Netw.* **2021**, *7*, 85–99. [CrossRef]
52. Liu, C.H.; Piao, C.; Tang, J. Energy-Efficient UAV Crowdsensing with Multiple Charging Stations by Deep Learning. In Proceedings of the IEEE INFOCOM 2020—IEEE Conference on Computer Communications, Toronto, ON, Canada, 6–9 July 2020; pp. 199–208. [CrossRef]
53. 3GPP RAN. RP-232745: RAN Chair's Summary of 5G-Advanced in Release 20. Technical Report, 3rd Generation Partnership Project, 2024. Available online: https://www.3gpp.org/ftp/tsg_ran/TSG_RAN/TSGR_102/Docs/RP-232745.zip (accessed on 8 January 2026).
54. ITU-R. *Rec. ITU-R M.2160-0; Framework and Overall Objectives of the Future Development of IMT for 2030 and Beyond*; Technical Report; International Telecommunication Union: Geneva, Switzerland, 2023.
55. NGMN Alliance. *6G Use Cases and Analysis*; Technical Report; Next Generation Mobile Networks Alliance: Dusseldorf, Germany, 2023.
56. Ericsson. *6G Spectrum: Enabling the Future Mobile Life Beyond 2030*; Technical Report, Ericsson White Paper; Ericsson: Stockholm, Sweden, 2024.
57. Zeng, Y.; Xu, J.; Zhang, R. Energy minimization for wireless communication with rotary-wing UAV. *IEEE Trans. Wirel. Commun.* **2019**, *18*, 2329–2345. [CrossRef]
58. Yang, Z.; Xu, W.; Shikh-Bahaei, M. Energy Efficient UAV Communication with Energy Harvesting. *IEEE Trans. Veh. Technol.* **2020**, *69*, 1913–1927. [CrossRef]
59. Yan, H.; Chen, Y.; Yang, S.H. New Energy Consumption Model for Rotary-Wing UAV Propulsion. *IEEE Wirel. Commun. Lett.* **2021**, *10*, 2009–2012. [CrossRef]
60. Gong, H.; Huang, B.; Jia, B.; Dai, H. Modeling Power Consumptions for Multirotor UAVs. *IEEE Trans. Aerosp. Electron. Syst.* **2023**, *59*, 7409–7422. [CrossRef]
61. Koch, L.; Buse, D.S.; Wegener, M.; Schoenberg, S.; Badalian, K.; Dressler, F.; Andert, J. Accurate physics-based modeling of electric vehicle energy consumption in the SUMO traffic microsimulator. In Proceedings of the 2021 IEEE International Intelligent Transportation Systems Conference (ITSC), Indianapolis, IN, USA, 19–22 September 2021; pp. 1650–1657. [CrossRef]
62. Lahmeri, M.A.; Kishk, M.A.; Alouini, M.S. Charging Techniques for UAV-Assisted Data Collection: Is Laser Power Beaming the Answer? *IEEE Commun. Mag.* **2022**, *60*, 50–56. [CrossRef]
63. Kirubakaran, B.; Hosek, J. Extending UAV's Operational Time through Laser Beam Charging: System Model Analysis. In Proceedings of the 2022 45th International Conference on Telecommunications and Signal Processing, TSP 2022, Prague, Czech Republic, 13–15 July 2022; pp. 322–328. [CrossRef]
64. Lee, Z.J.; Sharma, S.; Johansson, D.; Low, S.H. ACN-Sim: An Open-Source Simulator for Data-Driven Electric Vehicle Charging Research. In Proceedings of the 2019 IEEE International Conference on Communications, Control, and Computing Technologies for Smart Grids (SmartGridComm), Beijing, China, 21–23 October 2019.
65. SUMO. *Shortest or Optimal Path Routing–SUMO Documentation*; SUMO: Paris, France, 2025.
66. SAE International. *J2954B: Wireless Power Transfer for Light-Duty Plug-in/Electric Vehicles and Alignment Methodology*; SAE International: Warrendale, PA, USA, 2019.
67. Huh, J.; Lee, S.W.; Lee, W.Y.; Cho, G.H.; Rim, C.T. Narrow-width inductive power transfer system for online electrical vehicles. *IEEE Trans. Power Electron.* **2011**, *26*, 3666–3679. [CrossRef]
68. Gomes, Z.M.; Prado, E.O.; Gall, Y.L.; Damm, G.; Ripoll, C.; Pinheiro, J.R. Design, Model, and Control of a Dynamic Wireless Power Transfer System for a 30 kW Electric Vehicle Charger Application. *IEEE J. Emerg. Sel. Top. Power Electron.* **2025**, *13*, 3882–3894. [CrossRef]
69. Jonah, O.; Georgakopoulos, S.V. Wireless power transfer in concrete via strongly coupled magnetic resonance. *IEEE Trans. Antennas Propag.* **2013**, *61*, 1378–1384. [CrossRef]
70. Schulman, J.; Wolski, F.; Dhariwal, P.; Radford, A.; Klimov, O. Proximal Policy Optimization Algorithms. *arXiv* **2017**, arXiv:1707.06347. [CrossRef]

71. Haarnoja, T.; Zhou, A.; Abbeel, P.; Levine, S. Soft Actor-Critic: Off-Policy Maximum Entropy Deep Reinforcement Learning with a Stochastic Actor. In Proceedings of the 35th International Conference on Machine Learning (ICML 2018), Stockholm, Sweden, 10–15 July 2018; Volume 5, pp. 2976–2989.
72. Fujimoto, S.; Hoof, H.V.; Meger, D. Addressing Function Approximation Error in Actor-Critic Methods. In Proceedings of the 35th International Conference on Machine Learning, ICML 2018, Stockholm, Sweden, 10–15 July 2018; Volume 4, pp. 2587–2601.
73. Lillicrap, T.P.; Hunt, J.J.; Pritzel, A.; Heess, N.; Erez, T.; Tassa, Y.; Silver, D.; Wierstra, D. Continuous control with deep reinforcement learning. In Proceedings of the 4th International Conference on Learning Representations, ICLR 2016—Conference Track Proceedings, San Juan, Puerto Rico, 2–4 May 2016; pp. 1–14.
74. Ontario Energy Board. *Historical Electricity Rates*; Ontario Energy Board: Toronto, ON, Canada, 2025.
75. Ontario Energy Board. *Electricity Rates*; Ontario Energy Board: Toronto, ON, Canada, 2025.
76. SUMO. *SUMO Documentation*; SUMO: Paris, France, 2025. Available online: https://sumo.dlr.de/docs/ (accessed on 8 January 2026).
77. SUMO. *MMPEVEM—SUMO Documentation*; SUMO: Paris, France, 2025. Available online: https://sumo.dlr.de/docs/Models/MMPEVEM.html (accessed on 8 January 2026).
78. EV Database. *All Electric Vehicles in Europe*; EV Database: Amsterdam, The Netherlands, 2025.
79. Jain, R.; Chiu, D.M.; Hawe, W. *A Quantitative Measure of Fairness and Discrimination for Resource Allocation in Shared Computer Systems*; Technical Report TR-301; Digital Equipment Corporation, Eastern Research Laboratory: Hudson, MA, USA, 1984.

Disclaimer/Publisher's Note: The statements, opinions and data contained in all publications are solely those of the individual author(s) and contributor(s) and not of MDPI and/or the editor(s). MDPI and/or the editor(s) disclaim responsibility for any injury to people or property resulting from any ideas, methods, instructions or products referred to in the content.